Publication Year	2016
Acceptance in OA	2020-05-27T16:02:01Z
Title	Planck intermediate results. XXXII. The relative orientation between the magnetic field and structures traced by interstellar dust
Authors	Planck Collaboration, Adam, R., Ade, P. A. R., Aghanim, N., Alves, M. I. R., Arnaud, M., Arzoumanian, D., Ashdown, M., Aumont, J., Baccigalupi, C., Banday, A. J., GRUPPUSO, ALESSANDRO, Guillet, V., Hansen, F. K., Hanson, D., Harrison, D. L., Henrot-Versillé, S., Hernández-Monteagudo, C., Herranz, D., Hildebrandt, S. R., Leonardi, R., Sunyaev, R., Hivon, E., Hobson, M., Holmes, W. A., Hovest, W., Huffenberger, K. M., Hurier, G., Jaffe, A. H., Jaffe, T. R., Jones, W. C., Juvela, M., Sutton, D., Levrier, F., Keihänen, E., Keskitalo, R., Kisner, T. S., Kneissl, R., Barreiro, R. B., Liguori, M., Lilje, P. B., Linden-Vørnle, M., López-Caniego, M., Suur-Uski, A. -S., Lubin, P. M., Macías-Pérez, J. F., Maffei, B., Maino, D., Mandolesi, N., Maris, M., Bartolo, N., Marshall, D. J., Martin, P. G., Martínez-González, E., Sygnet, J. -F., Masi, S., Matarrese, S., Mazzotta, P., Melchiorri, A., Mendes, L., Mennella, A., Migliaccio, M., Battaner, E., Miville-Deschênes, M. -A., Moneti, A., Tauber, J. A., Montier, L., MORGANTE, GIANLUCA, Mortlock, D., Munshi, D., Murphy, J. A., Naselsky, P., Natoli, P., Nørgaard-Nielsen, H. U., Benabed, K., Noviello, F., Terenzi, L., Novikov, D., Novikov, I., Oppermann, N., Oxborrow, C. A., Pagano, L., Pajot, F., PAOLETTI, DANIELA, Pasian, F., Perdereau, O., Benoit-Lévy, A., Toffolatti, L., Perotto, L., Perrotta, F., Pettorino, V., Piacentini, F., Piat, M., Plaszczynski, S., Pointecouteau, E., Polenta, G., Ponthieu, N., Popa, L., Tomasi, M., Bernard, J. -P., Pratt, G. W., Prunet, S., Puget, J. -L., Rachen, J. P., Reach, W. T., Reinecke, M., Remazeilles, M., Renault, C., Ristorcelli, I., Tristram, M., Rocha, G., Bersanelli, M., Roudier, G., Rubiño-Martín, J. A., Rusholme, B., SANDRI, MAURA, Santos, D., Savini, G., Scott, D., Soler, J. D., Bonaldi, A., Spencer, L. D., Stolyarov, V., Bielewicz, P., Sudiwala, R., Knoche, J., Tucci, M., UMANA, Grazia Maria Gloria, VALENZIANO, LUCA, Valiviita, J., Van Tent, B., Vielva, P., VILLA, FABRIZIO, Wade, L. A., Wandelt, B. D., Wehus, I. K., Kunz, M., Bonavera, L., Wiesemeyer, H., Yvon, D., ZACCHEI, Andrea, Zonca, A., Bond, J. R., Borrill, J., Bouchet, F. R., Boulanger, F., Bracco, A., Kurki-Suonio, H., BURIGANA, CARLO, Butler, R. C., Calabrese, E., Cardoso, J. -F., Catalano, A., Chamballu, A., Chiang, H. C., Christensen, P. R., Colombi, S., Colombo, L. P. L., Lagache, G., Combet, C., Couchot, F., Crill, B. P., Curto, A., CUTTAIA, FRANCESCO, Danese, L., Davies, R. D., Davis, R. J., de Bernardis, P., De Rosa, A., Lamarre, J. -M., de Zotti, G., Delabrouille, J., Dickinson, C., Diego, J. M., Dole, H., Donzelli, S., Doré, O., Douspis, M., Ducout, A., Dupac, X., Lasenby, A., Efstathiou, G., Elsner, F., Enßlin, T. A., Eriksen, H. K., Falgarone, E., Ferrière, K., FINELLI, FABIO, Forni, O., Frailis, M., Fraisse, A. A., Lattanzi, M., FRANCESCHI, ENRICO, Frejsel, A., GALEOTTA, Samuele, Galli, S., Ganga, K., Ghosh, T., Giard, M., Gjerløw, E., González-Nuevo, J., Górski, K. M., Lawrence, C. R.,

Astronomy & Astrophysics manuscript no. PIPXXXII
October 22, 2018

Planck intermediate results. XXXII. The relative orientation between the magnetic field and structures traced by interstellar dust

Planck Collaboration: R. Adam[68], P. A. R. Ade[79], N. Aghanim[54], M. I. R. Alves[54], M. Arnaud[66], D. Arzoumanian[54], M. Ashdown[63,6], J. Aumont[54], C. Baccigalupi[78], A. J. Banday[85,10], R. B. Barreiro[60], N. Bartolo[27], E. Battaner[87,88], K. Benabed[55,84], A. Benoit-Lévy[21,55,84], J.-P. Bernard[85,10], M. Bersanelli[30,46], P. Bielewicz[85,10,78], A. Bonaldi[62], L. Bonavera[60], J. R. Bond[9], J. Borrill[13,81], F. R. Bouchet[55,84], F. Boulanger[54], A. Bracco[54], C. Burigana[45,28,47], R. C. Butler[45], E. Calabrese[83], J.-F. Cardoso[67,1,55], A. Catalano[68,65], A. Chamballu[66,14,54], H. C. Chiang[24,7], P. R. Christensen[75,33], S. Colombi[55,84], L. P. L. Colombo[20,61], C. Combet[68], F. Couchot[64], B. P. Crill[61,76], A. Curto[6,60], F. Cuttaia[45], L. Danese[78], R. D. Davies[62], R. J. Davis[62], P. de Bernardis[29], A. de Rosa[45], G. de Zotti[42,78], J. Delabrouille[1], C. Dickinson[62], J. M. Diego[60], H. Dole[54,53], S. Donzelli[46], O. Doré[61,11], M. Douspis[54], A. Ducout[55,51], X. Dupac[36], G. Efstathiou[57], F. Elsner[55,84], T. A. Enßlin[71], H. K. Eriksen[58], E. Falgarone[65], K. Ferrière[85,10], F. Finelli[45,47], O. Forni[85,10], M. Frailis[44], A. A. Fraisse[24], E. Franceschi[45], A. Frejsel[75], S. Galeotta[44], S. Galli[55], K. Ganga[1], T. Ghosh[54], M. Giard[85,10], E. Gjerløw[58], J. González-Nuevo[60,78], K. M. Górski[61,89], A. Gregorio[31,44,49], A. Gruppuso[45], V. Guillet[54], F. K. Hansen[58], D. Hanson[73,61,9], D. L. Harrison[57,63], S. Henrot-Versillé[64], C. Hernández-Monteagudo[12,71], D. Herranz[60], S. R. Hildebrandt[61], E. Hivon[55,84], M. Hobson[6], W. A. Holmes[61], W. Hovest[71], K. M. Huffenberger[22], G. Hurier[54], A. H. Jaffe[51], T. R. Jaffe[85,10], W. C. Jones[24], M. Juvela[23], E. Keihänen[23], R. Keskitalo[13], T. S. Kisner[70], R. Kneissl[35,8], J. Knoche[71], M. Kunz[16,54,2], H. Kurki-Suonio[23,40], G. Lagache[5,54], J.-M. Lamarre[65], A. Lasenby[6,63], M. Lattanzi[28], C. R. Lawrence[61], R. Leonardi[36], F. Levrier[65], M. Liguori[27], P. B. Lilje[58], M. Linden-Vørnle[15], M. López-Caniego[60], P. M. Lubin[25], J. F. Macías-Pérez[68], B. Maffei[62], D. Maino[30,46], N. Mandolesi[45,4,28], M. Maris[44], D. J. Marshall[66], P. G. Martin[9], E. Martínez-González[60], S. Masi[29], S. Matarrese[27], P. Mazzotta[32], A. Melchiorri[29,48], L. Mendes[36], A. Mennella[30,46], M. Migliaccio[57,63], M.-A. Miville-Deschênes[54,9], A. Moneti[55], L. Montier[85,10], G. Morgante[45], D. Mortlock[51], D. Munshi[79], J. A. Murphy[74], P. Naselsky[75,33], P. Natoli[28,3,45], H. U. Nørgaard-Nielsen[15], F. Noviello[62], D. Novikov[51], I. Novikov[75], N. Oppermann[9], C. A. Oxborrow[15], L. Pagano[29,48], F. Pajot[54], D. Paoletti[45,47], F. Pasian[44], O. Perdereau[64], L. Perotto[68], F. Perrotta[78], V. Pettorino[39], F. Piacentini[29], M. Piat[1], S. Plaszczynski[64], E. Pointecouteau[85,10], G. Polenta[3,43], N. Ponthieu[54,50], L. Popa[56], G. W. Pratt[66], S. Prunet[55,84], J.-L. Puget[54], J. P. Rachen[18,71], W. T. Reach[86], M. Reinecke[71], M. Remazeilles[62,54,1], C. Renault[68], I. Ristorcelli[85,10], G. Rocha[61,11], G. Roudier[1,65,61], J. A. Rubiño-Martín[59,34], B. Rusholme[52], M. Sandri[45], D. Santos[68], G. Savini[77], D. Scott[19], J. D. Soler[54], L. D. Spencer[79], V. Stolyarov[6,63,82], R. Sudiwala[79], R. Sunyaev[71,80], D. Sutton[57,63], A.-S. Suur-Uski[23,40], J.-F. Sygnet[55], J. A. Tauber[37], L. Terenzi[38,45], L. Toffolatti[17,60,45], M. Tomasi[30,46], M. Tristram[64], M. Tucci[16,64], G. Umana[41], L. Valenziano[45], J. Valiviita[23,40], B. Van Tent[69], P. Vielva[60], F. Villa[45], L. A. Wade[61], B. D. Wandelt[55,84,26], I. K. Wehus[61], H. Wiesemeyer[72], D. Yvon[14], A. Zacchei[44], and A. Zonca[25]

(Affiliations can be found after the references)

Preprint online version: October 22, 2018

ABSTRACT

The role of the magnetic field in the formation of the filamentary structures observed in the interstellar medium (ISM) is a debated topic owing to the paucity of relevant observations needed to test existing models. The *Planck* all-sky maps of linearly polarized emission from dust at 353 GHz provide the required combination of imaging and statistics to study the correlation between the structures of the Galactic magnetic field and of interstellar matter over the whole sky, both in the diffuse ISM and in molecular clouds. The data reveal that structures, or ridges, in the intensity map have counterparts in the Stokes Q and/or U maps. We focus our study on structures at intermediate and high Galactic latitudes, which cover two orders of magnitude in column density, from 10^{20} to 10^{22} cm^{-2}. We measure the magnetic field orientation on the plane of the sky from the polarization data, and present an algorithm to estimate the orientation of the ridges from the dust intensity map. We use analytical models to account for projection effects. Comparing polarization angles on and off the structures, we estimate the mean ratio between the strengths of the turbulent and mean components of the magnetic field to be between 0.6 and 1.0, with a preferred value of 0.8. We find that the ridges are usually aligned with the magnetic field measured on the structures. This statistical trend becomes more striking for increasing polarization fraction and decreasing column density. There is no alignment for the highest column density ridges. We interpret the increase in alignment with polarization fraction as a consequence of projection effects. We present maps to show that the decrease in alignment for high column density is not due to a loss of correlation between the distribution of matter and the geometry of the magnetic field. In molecular complexes, we also observe structures perpendicular to the magnetic field, which, statistically, cannot be accounted for by projection effects. This first statistical study of the relative orientation between the matter structures and the magnetic field in the ISM points out that, at the angular scales probed by *Planck*, the field geometry projected on the plane of the sky is correlated with the distribution of matter. In the diffuse ISM, the structures of matter are usually aligned with the magnetic field, while perpendicular structures appear in molecular clouds. We discuss our results in the context of models and MHD simulations, which attempt to describe the respective roles of turbulence, magnetic field, and self-gravity in the formation of structures in the magnetized ISM.

Key words. ISM: clouds – ISM: Magnetic Fields – ISM: structure – Magnetohydrodynamics – Polarization – Turbulence

1. Introduction

The filamentary appearance of the interstellar medium (ISM) has been revealed over the last decades by observations of dust emission, stellar reddening, and gas line emission, mainly CO and H I (see Hennebelle & Falgarone 2012, for a recent ISM review). Most recently, *Herschel* maps of dust emission at far-infrared wavelengths have identified gravitationally bound filaments as the loci where stars form (André et al. 2010). Filaments are ubiquitous in interstellar space and are essential to star formation, but our understanding of how they form is still fragmentary.

Filaments are striking features in numerical simulations of the diffuse ISM and molecular clouds (e.g. Heitsch et al. 2005; Nakamura & Li 2008; Gong & Ostriker 2011; Hennebelle 2013). They are present in both hydrodynamic and magneto-hydrodynamic (MHD) simulations, but they are more conspicuous in the latter. These studies relate the filamentary appearance of the ISM to compression and shear driven by turbulence, and the anisotropic infall of gravitationally unstable structures. Soler et al. (2013) find that, statistically, the orientation changes from parallel to perpendicular for gravitationally bound structures in simulations where the magnetic field is dynamically important.

The role of the magnetic field in the ISM dynamics depends on the field strength with respect to gravitational and turbulent energies. In the diffuse ISM, the magnetic energy is observed to be comparable with the turbulent kinetic energy of the gas (Heiles & Troland 2005; Basu & Roy 2013) and to dominate its self-gravity (Crutcher et al. 2010), while stars form where and when gravity prevails. On what spatial and time scales does this transition in the ratio between magnetic and gravitational energies occur? This question has been addressed by theorists in several ways. Ambipolar diffusion (Ciolek & Mouschovias 1993), including turbulence (Zweibel 2002) or magnetic reconnection (Lazarian & Vishniac 1999), can decouple matter from the magnetic field. Furthermore, gas motions along field lines contribute to condensing the matter without increasing the magnetic flux. This has been suggested for the formation of molecular clouds (Blitz & Shu 1980; Hartmann et al. 2001; Hennebelle et al. 2008; Heitsch et al. 2009; Inoue & Inutsuka 2009) and of gravitationally bound filaments within gas sheets (Nagai et al. 1998). Because of magnetic tension (Hennebelle & Pérault 2000; Heyer & Brunt 2012), the gas is expected to flow mainly along field lines where turbulence is sub-Alfvénic.

The challenge faced by observers is to gather the data necessary to characterize the interplay between gravity, turbulence, and magnetic fields from the diffuse ISM to star-forming molecular clouds. A wealth of data is already available to quantify the gas self-gravity and turbulence (Hennebelle & Falgarone 2012), but we have comparatively little information on the magnetic field strength and its structure within interstellar clouds. The dearth of data on the magnetic field follows from the difficulty of performing the relevant observations. Measurements of the magnetic field components along the line of sight and on the plane of the sky using the Zeeman effect and dust and synchrotron linear polarizations, respectively, are notoriously difficult (Crutcher 2012; Haverkorn 2015).

Synchrotron emission and Faraday rotation have been used to estimate the strength of the magnetic field and the ratio between its random and regular components in the Milky Way and external galaxies (Haverkorn et al. 2004; Beck 2007; Schnitzeler et al. 2007; Houde et al. 2013). A spatial correlation between the magnetic field structure and that of interstellar matter has been observed at kpc-scales in external galaxies from synchrotron radio polarization (Beck et al. 2005; Patrikeev et al. 2006; Fletcher et al. 2011). This correlation has been observed to depend on the gas density and star formation rate (Chyży 2008). However, the interplay between the structure of the field and that of matter on smaller scales in the solar neighbourhood is still highly debated.

A number of studies, using the polarization of background starlight caused by dichroic absorption, have targeted filaments in dark clouds (e.g. Goodman et al. 1990, 1995; Pereyra & Magalhães 2004; Alves et al. 2008; Chapman et al. 2011; Cashman & Clemens 2014), and in the diffuse ISM at lower column densities (McClure-Griffiths et al. 2006; Clark et al. 2014). Studying the relative orientation between the main axis of elongated molecular clouds and the orientation of the magnetic field inferred from starlight polarimetry, Li et al. (2013) present evidence for a bimodal distribution of relative orientations being either parallel or perpendicular. Most of these studies rely on polarization observations for discrete lines of sight selected by the availability of background stars, and often the magnetic field orientation is not measured at the position of the matter structures but on nearby lines of sight.

The *Planck*[1] satellite has recently completed the first all-sky map of dust polarization in emission. This is an immense step forward in brightness sensitivity and statistics from earlier polarization observations at sub-mm wavelengths (e.g. Benoît et al. 2004; Ward-Thompson et al. 2009; Koch et al. 2010; Poidevin et al. 2014; Matthews et al. 2014). While only ground-based observations provide the angular resolution required to measure the polarization of pre-stellar cores (Matthews et al. 2009; Tang et al. 2009) and to image dust polarization in distant molecular clouds (Li et al. 2006; Tassis et al. 2009), the *Planck* data are unique in their ability to map the dust polarization of filamentary structures in the solar neighbourhood. For the first time, we have the data needed to characterize statistically the structure of the Galactic magnetic field and its coupling to interstellar matter and turbulence at physical scales relevant to the formation of interstellar filaments.

The data are revealing a new view of the sky that we have started to explore. A first description of the *Planck* polarization maps at 353 GHz is presented in Planck Collaboration Int. XIX (2014) and Planck Collaboration Int. XX (2014). These first two papers describe the statistics of the polarization angle ψ (perpendicular to the magnetic field orientation projected on the plane of the sky) and polarization fraction p. Planck Collaboration Int. XX (2014) show that the statistics of the data on ψ and p compare well with those measured on a MHD simulation of a molecular cloud formed at the interface of two colliding flows. A major finding of this paper is that the statistics of ψ and p depend on the direction of the mean magnetic field. Here, we pursue our analysis of the *Planck* dust polarization sky, focusing on the polarization properties of the localized filamentary structures in the solar neighbourhood, alternatively called ridges, identified in the Stokes I map. We use the *Planck* data to determine and compare the orientation of the filamentary structures and that of the magnetic field projected on the plane of the sky.

The paper is organized as follows. The *Planck* data we use are introduced in Sect. 2. Section 3 presents sky images that emphasize the correlation between structures in polarization and corresponding features in intensity. The selection and charac-

[1] *Planck* (`http://www.esa.int/Planck`) is a project of the European Space Agency (ESA) with instruments provided by two scientific consortia funded by ESA member states (in particular the lead countries France and Italy), with contributions from NASA (USA) and telescope reflectors provided by a collaboration between ESA and a scientific consortium led and funded by Denmark.

teristics of the regions where we compare the orientations of the magnetic field and that of the structures of matter are described in Sect. 4. Section 5 presents the magnetic field properties of the selected structures. Sections 6 and 7 focus on quantifying the relative orientation of the magnetic field and the ridges in the diffuse ISM and molecular clouds. We discuss our results in the context of our present understanding of the formation of structures in the magnetized ISM in Sect. 8. The main results are summarized in Sect. 9. The paper has two appendices. Appendix A details how we measure the local orientation of the structures in the dust emission map and quantify uncertainties. In Appendix B, we present the model that we use to quantify projection effects and interpret the statistics of the angle between the magnetic field and the brightness ridges on the sky.

2. Data Sets

Planck observed the sky polarization in seven frequency bands from 30 to 353 GHz (Planck Collaboration I 2014). In this paper, we only use the data from the High Frequency Instrument (HFI, Lamarre et al. 2010) at the highest frequency, 353 GHz, where the dust emission is the brightest. This is the best-suited *Planck* map for studying the structure of the dust polarization sky (Planck Collaboration Int. XIX 2014; Planck Collaboration Int. XX 2014).

We use the Stokes Q and U maps and the associated noise maps made with the five independent consecutive sky surveys of the *Planck* cryogenic mission, which correspond to the DR3 (delta-DX9) internal data release. We refer to previous *Planck* publications for the data processing, map-making, photometric calibration, and photometric uncertainties (Planck Collaboration II 2014; Planck Collaboration VI 2014; Planck Collaboration V 2014; Planck Collaboration VIII 2014). The Q and U maps are corrected for spectral leakage as described in Planck Collaboration Int. XIX (2014). As in this first *Planck* polarization paper, we use the IAU convention for the polarization angle, measured from the local direction to the north Galactic pole with positive values towards the east.

For the dust total intensity at 353 GHz we use the model map, D_{353}, and the associated noise map, derived from a fit with a modified blackbody of the *Planck* data at $\nu \geq 353$ GHz, and *IRAS* at $\lambda = 100\,\mu$m (Planck Collaboration XI 2014). This map has a lower noise than the corresponding 353 GHz Stokes I *Planck* map. Furthermore, D_{353} is the dust specific intensity corrected for zodiacal emission, cosmic microwave background anisotropies, and the cosmic infrared background monopole.

The Q and U maps are initially at $4\farcm8$ resolution, and D_{353} at $5'$. The three maps are in `HEALPix` format[2] with a pixelization $N_{\rm side} = 2048$. To increase the signal-to-noise ratio of extended emission, we smooth the three maps to $15'$ resolution using the Gaussian approximation to the *Planck* beam. We reduce the `HEALPix` resolution to $N_{\rm side} = 512$ ($7\farcm1$ pixels) after smoothing. To finely sample the beam, we also use the smoothed D_{353} map with $N_{\rm side} = 1024$ in Appendix A. For the polarization maps, we apply the "`ismoothing`" routine of `HEALPix` that decomposes the Q and U maps into E and B maps, applies the Gaussian smoothing in harmonic space, and transforms the smoothed E and B back into Q and U maps at $N_{\rm side} = 512$ resolution. Most of our analysis is based on the Q, U, and D_{353} maps, but we also use the maps of the de-biased polarization fraction p and angle ψ produced by Planck Collaboration Int. XIX (2014).

[2] Górski et al. (2005), `http://healpix.sf.net`

The contribution of the CMB polarization to the Q and U maps at 353 GHz is negligible for this study.

3. Structures in the polarization maps

We introduce dust polarization (Sect. 3.1) and present all-sky images highlighting localized structures in the dust Stokes Q and U maps correlated with corresponding features in intensity (Sect. 3.2).

3.1. Dust polarization over the sky

The integral equations of the Stokes parameters for linear dust polarization are defined in Planck Collaboration Int. XX (2014) (their Eqs. 5 to 7). For constant magnetic field orientation and polarization fraction along the line of sight, the Q and U parameters can be related to the total intensity, I , through

$$\begin{aligned} Q &= p_0\, \cos^2\gamma \cos(2\,\psi)\, I, \\ U &= p_0\, \cos^2\gamma \sin(2\,\psi)\, I, \end{aligned} \tag{1}$$

where γ is the angle between the magnetic field and the plane of the sky and ψ the polarization angle. The intrinsic polarization fraction of dust emission, p_0, is given by

$$p_0 = \frac{C_{\rm pol}}{C_{\rm avg}}\, R, \tag{2}$$

where $C_{\rm pol}$ and $C_{\rm avg}$ are the polarization and the average cross-sections of dust, as defined in Appendix B of Planck Collaboration Int. XX (2014), and R is the Rayleigh reduction factor, which characterizes the degree of dust grain alignment with the local magnetic field (Lee & Draine 1985; Hildebrand 1988). The observed polarization fraction is

$$p = p_0 \cos^2\gamma. \tag{3}$$

From Eq. (1), the localized structures in maps of dust polarization can come either from local variations of the magnetic field orientation, the intrinsic polarization fraction p_0, or the total emission I map. The structure of the polarization sky also depends on the depolarization associated with the magnetic field structure in the volume sampled by the beam (Lee & Draine 1985; Planck Collaboration Int. XX 2014), which is ignored in Eq. (1). The filamentary structures revealed by the maps of the local dispersion of the polarization angle, presented in Planck Collaboration Int. XIX (2014) and Planck Collaboration Int. XX (2014), are structures associated with changes in the orientation of the magnetic field because they do not correlate with structures in the dust I map. As pointed out by Planck Collaboration Int. XIX (2014), these structures morphologically resemble those found in maps of normalized gradients of polarized synchrotron emission at radio frequencies (Burkhart et al. 2012; Iacobelli et al. 2014).

On the other hand, this paper presents a complementary analysis of the *Planck* polarization sky, focusing on structures that have a counterpart in the I map.

3.2. Visualization of the structures

Henceforth, we use Eq. (1) with the D_{353} map for the total intensity I, and the Q and U maps at 353 GHz, which we write as Q_{353} and U_{353}. We consider localized structures, which appear in the D_{353} map as contrasted ridges with respect to the local and

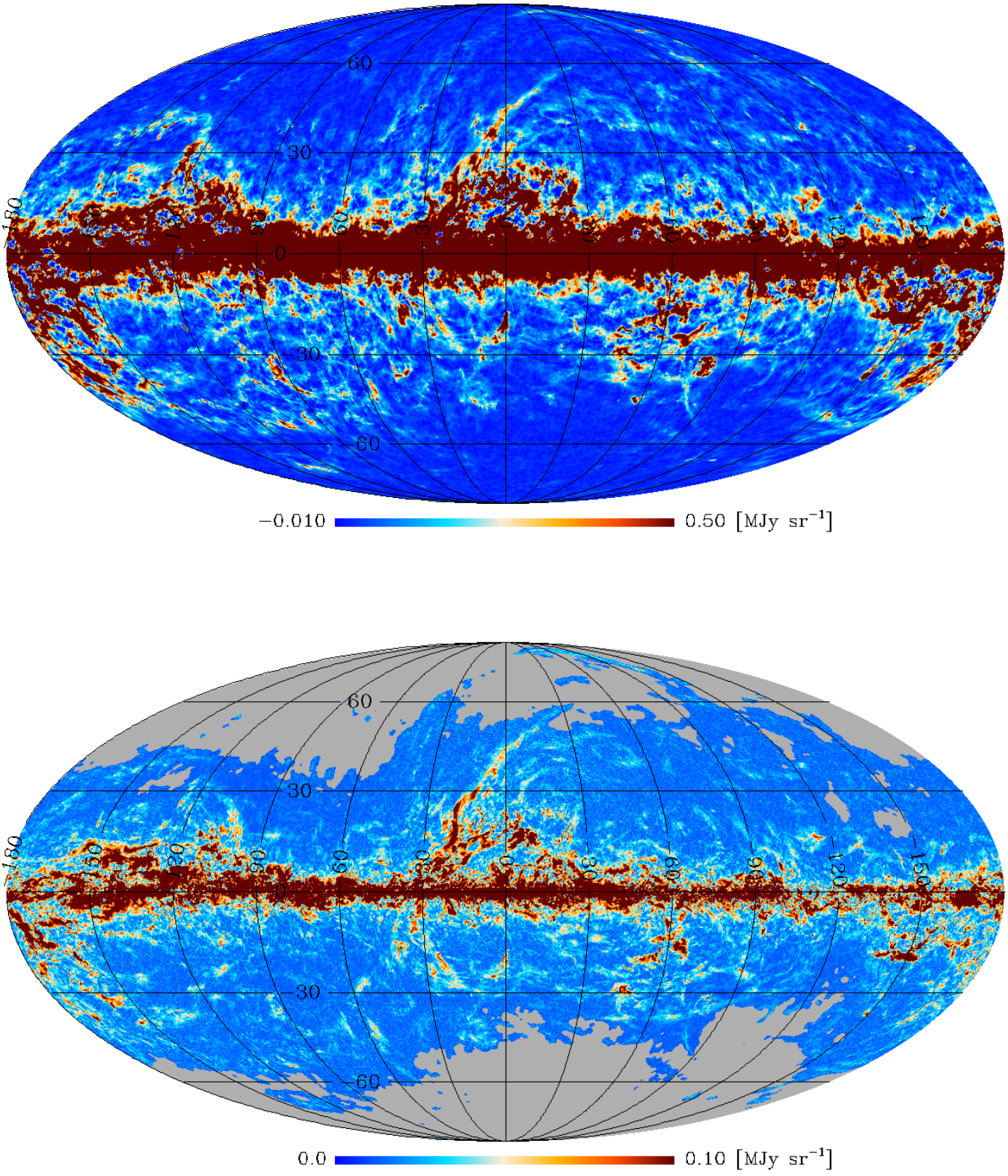

Fig. 1. *Top:* all-sky Mollweide display of the dust emission intensity at 353 GHz after background subtraction, $D_{353}^{\rm Dif}$ (see Sect. 3.2). *Bottom:* corresponding difference map for the polarized emission, $P_{353}^{\rm Dif}$ in Eq. (6). The regions of low polarization signal at high Galactic latitude are masked. These images include a grid of Galactic coordinates in degrees.

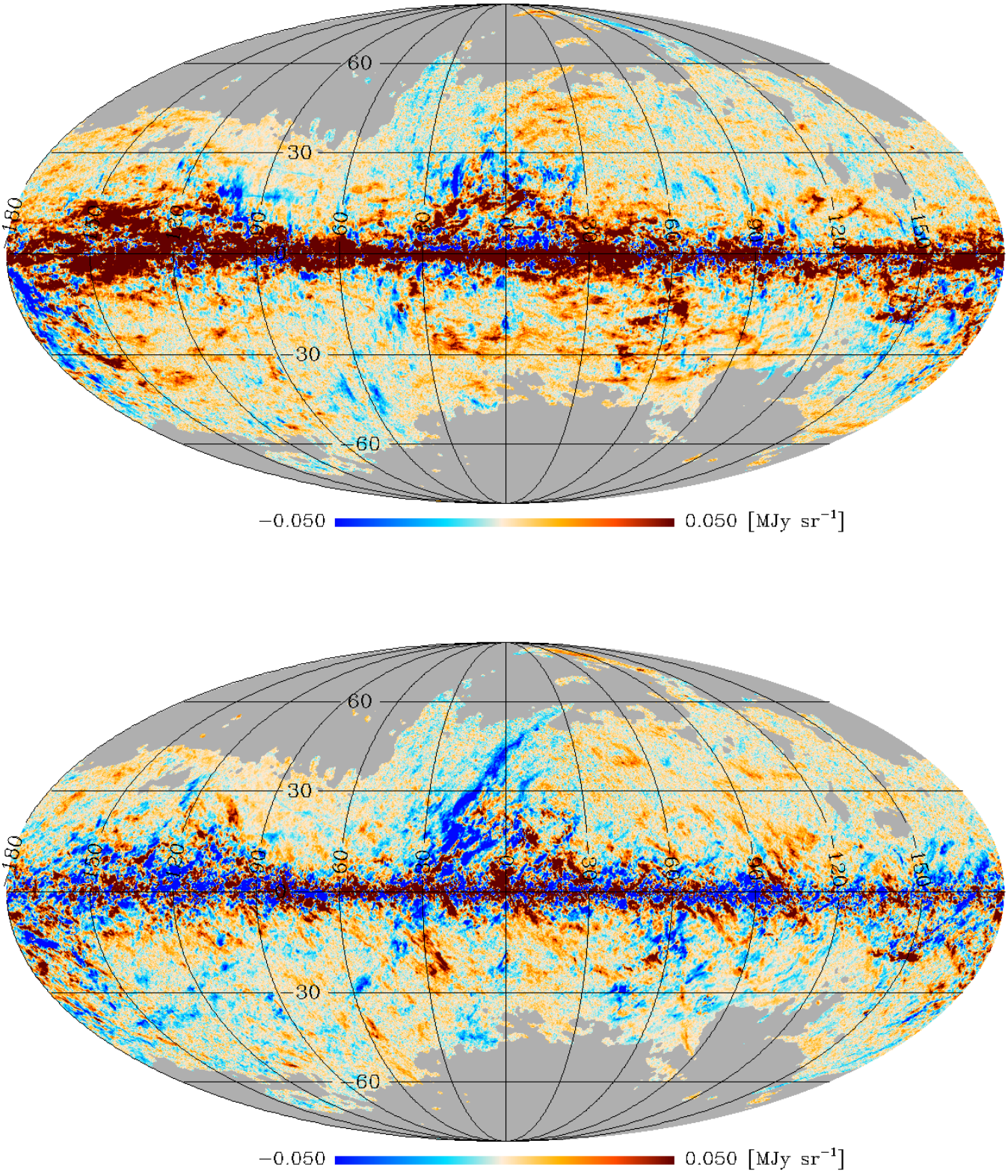

Fig. 2. All-sky Mollweide display of the Stokes maps $Q_{353}^{\rm Dif}$ (*top*) and $U_{353}^{\rm Dif}$ (*bottom*) at 353 GHz after background subtraction. The regions of low polarization signal at high Galactic latitude are masked. These images include a grid of Galactic coordinates in degrees. The map shown in the bottom panel represents the Stokes U parameter in `HEALPix` convention, which corresponds to $-U$ in IAU convention, as described in Eq. (1).

more diffuse emission, hereafter referred to as the background. Previous works at radio frequencies already faced the problem of separating the signal of localized structures in the Galaxy from the background emission. Sofue & Reich (1979) introduced the unsharp-mask method to investigate the structure of the North Polar Spur from radio continuum observations at 1420 MHz obtained with the 100-m telescope. To present the contrasted structures we follow a similar, but simpler, approach.

We produce a low resolution background map, $D_{353}^{\rm BG}$, from D_{353}. For each sky pixel, we compute a histogram of D_{353} within a circular aperture of radius 2.°5 (this is not a critical value of the data analysis, repeating the background estimate with an aperture of 5° does not significantly change our results). The background value at this position is estimated from the mean of the 20 % lowest values. We also show that our choice of the 20 % fraction is not a critical aspect of the data analysis in Sects. 5 and 6.1. The top panel in Fig. 1 shows the difference

$$D_{353}^{\rm Dif} = D_{353} - D_{353}^{\rm BG}, \tag{4}$$

which highlights localized features in the sky from low to high Galactic latitudes.

We also make the background maps, $Q_{353}^{\rm BG}$ and $U_{353}^{\rm BG}$, computing the mean values of the Q_{353} and U_{353} maps over the same pixels used to compute $D_{353}^{\rm BG}$, as well as the difference maps for the Stokes parameters

$$\begin{aligned} Q_{353}^{\rm Dif} &= Q_{353} - Q_{353}^{\rm BG} \\ U_{353}^{\rm Dif} &= U_{353} - U_{353}^{\rm BG}. \end{aligned} \tag{5}$$

The $Q_{353}^{\rm Dif}$ and $U_{353}^{\rm Dif}$ maps are presented in Fig. 2. The results of the background subtraction on the polarization data are illustrated by the map defined by

$$P_{353}^{\rm Dif} = \sqrt{(Q_{353}^{\rm Dif})^2 + (U_{353}^{\rm Dif})^2}, \tag{6}$$

shown in the bottom panel of Fig. 1. We present the maps after applying the same all-sky mask defined in Planck Collaboration Int. XIX (2014). They show pixels where the systematic uncertainties are small, and where the dust signal dominates the total emission (see Sect. 2.4 of Planck Collaboration Int. XIX 2014). We note that $P_{353}^{\rm Dif}$ is only used for visualization purposes, and we stress that it is not used for data analysis. In the data analysis we make use of the polarization fraction map described by Planck Collaboration Int. XIX (2014) (see Sect. 2), which is corrected for the positive bias due to noise.

The polarization maps show localized structures that are spatially coincident with comparable features in $D_{353}^{\rm Dif}$. However, there is not a one-to-one correspondence between the polarization and intensity maps. The localized features in $D_{353}^{\rm Dif}$ appear with different contrast and sign in the polarization maps. These differences trace changes in the polarization fraction and angle, which are observed to vary.

4. Ridges in the dust emission map

In this section we describe how we identify and select the ridges in the D_{353} map, where we will later compare the orientation of the magnetic field and that of the matter structures (Sects. 4.1 and 4.2). The selected structures are characterized in Sect. 4.3.

4.1. Detection of the ridges

Deciding where to compare the orientations of the magnetic field and structures of matter is an important step of our data analysis. We need an algorithm that selects pixels on localized structures, providing the orientation at each position on the sky. Thus, unlike what was done in analysing *Herschel* maps of molecular clouds in the Gould Belt (Arzoumanian et al. 2011), we do not seek to identify filaments as coherent structures, and we do not need to restrict the analysis to the crest of the filaments.

Anisotropic wavelet techniques, like those applied by Patrikeev et al. (2006) to investigate the spiral arms of M51, can be used to measure the relative orientation between the magnetic field and the matter structure, although they are not optimal for tracing complicated and intricate patterns.

These distinct requirements led us to make use of a different algorithm than that applied in these earlier studies. To identify the structures, we use a Hessian analysis of D_{353}. The Hessian matrix was also used to analyse *Herschel* images of the L1641 cloud in Orion (Polychroni et al. 2013), and is related to analyses of the *cosmic-web* in cosmological large-scale structures (Pogosyan et al. 2009). This algorithm detects elongated ridges using a local determination of the curvature of the dust emission intensity. We compute the Hessian matrix of the unfiltered D_{353} map (the estimate of the local curvature is independent of the background subtraction). For each pixel of this map, we estimate the first and second derivatives with respect to the local Galactic coordinates (l, b) in order to build the corresponding Hessian matrix,

$$H(x,y) \equiv \begin{pmatrix} H_{xx} & H_{xy} \\ H_{yx} & H_{yy} \end{pmatrix}, \tag{7}$$

where x and y refer to the Galactic coordinates (l, b) as $x = b$ and $y = l \cos b$, so that the x-axis is pointing towards the north Galactic pole. The second-order partial derivatives are $H_{xx} = \partial^2 D_{353}/\partial x^2$, $H_{xy} = \partial^2 D_{353}/\partial x \partial y$, $H_{yx} = \partial^2 D_{353}/\partial y \partial x$, $H_{yy} = \partial^2 D_{353}/\partial y^2$. The Hessian matrix would be nearly the same if we used $D_{353}^{\rm Dif}$ instead of D_{353}. Indeed, the difference between the two maps, $D_{353}^{\rm BG}$, does not have significant structure at the scales over which the derivatives are computed.

By solving the characteristic equation of the Hessian matrix, we find the two eigenvalues,

$$\lambda_{\pm} = \frac{(H_{xx} + H_{yy}) \pm \sqrt{(H_{xx} - H_{yy})^2 + 4 H_{xy} H_{yx}}}{2}. \tag{8}$$

The two eigenvalues define the local curvature of the intensity. The map of the minimum eigenvalue, λ_-, shown in the upper panel of Fig. 3, highlights filamentary structures in D_{353}. The Hessian matrix encodes the information about the local orientation of the ridges. The angle between the north direction and the eigenvector corresponding to λ_- is perpendicular to the orientation angle θ of the crest of the ridge with respect to the north Galactic pole. This angle θ can be derived as

$$\theta = \frac{1}{2} \tan^{-1} \frac{H_{xy} + H_{yx}}{H_{xx} - H_{yy}}. \tag{9}$$

The computation of the orientation angle θ and its uncertainty, over the whole sky, is detailed in Appendix A. The Appendix also presents an independent algorithm, based on a method used by Hennebelle (2013) to analyse results from numerical simulations, where the orientation of structures is computed from the inertia matrix of the dust D_{353} map. The two independent estimates of the orientation angle are in good agreement.

4.2. Selection procedure

The λ_- curvature map highlights a complex bundle of filamentary structures, where the most significant ridges in D_{353} intersect underlying features owing to noise and background emission. To select interstellar matter structures, we build a mask based on three local criteria: intensity contrast with respect to the background map $D_{353}^{\rm BG}$, curvature and signal-to-noise of the polarization fraction. The Magellanic Clouds and the Galactic plane within $\pm 5^\circ$ in latitude are masked to focus on structures located in the solar neighbourhood. Hereafter, the masked pixels are the ones that we do not consider in the analysis. We also mask single-pixel regions produced by the selection criteria. Our final sample of ridges amounts to 4 % of the sky.

The details of the masking procedure are discussed in Appendix A. Here, we give a description of the main points. The first criterion defines a structure as a contrasted ridge in D_{353} with respect to the local background. We introduce a threshold, ζ, on the brightness contrast: $D_{353}^{\rm Dif}/D_{353}^{\rm BG} > \zeta$. We set $\zeta = 1$ and checked that changing the value of ζ to 0.5 or 2 does not change our statistical results.

The second criterion eliminates the contribution of background emission to the curvature. We use a toy model of the sky to define a threshold, $C_{\rm T}$, which depends on the brightness of the background (see Eq. (A.2) in Appendix A), on the negative curvature: $\lambda_- < -C_{\rm T}$. This criterion has its main impact at high Galactic latitudes.

The third selection criterion ensures a sufficient accuracy in the polarization angle. The uncertainty in the polarization angle directly depends on the uncertainty in polarized intensity P (see Eq. (B.5) in Planck Collaboration Int. XIX 2014); however, $p/\sigma_p \approx P/\sigma_P$ (where p and σ_p are the polarization fraction and the corresponding error described in Planck Collaboration Int. XIX (2014)), when $D_{353}/\sigma_{D_{353}} \gg P/\sigma_P$, which is true for all the pixels that meet our first two criteria. Thus, we select pixels with $p/\sigma_p > 3$, so that the uncertainties in the polarization angle are smaller than 10°, with a median value of 3°.

Two figures illustrate the selection procedure. The bottom panel in Fig. 3 presents the all-sky curvature map, where only the selected pixels are shown. As can be seen, our procedure does not bias the selection of the structures towards specific regions in the sky, but covers a wide range of Galactic latitudes. Figure 4 illustrates an expanded view of the Chamaeleon complex, highlighting the selected ridges in D_{353}.

Figure 5 shows the distribution function (DF) of the orientation angle θ from Eq. (9) for the selected structures as a function of Galactic latitude. The normalization of the DF is done by dividing the number of ridges in each bin of θ by the total number of selected ridges within each latitude bin. This total number is the same for all latitude bins. The DF does not present any preferred orientation of the structures in the northern hemisphere, but there is a slight dip at $\theta = 0^\circ$ in the southern hemisphere, most noticeable for the highest latitudes.

4.3. Characterization of ridges

For each selected pixel, we compute the excess column density defined as

$$\Delta N_{\rm H} = N_{\rm H}\,\frac{D_{353}^{\rm Dif}}{D_{353}} = 8.7\times10^{25}\,\tau_{353}\,\frac{D_{353}^{\rm Dif}}{D_{353}}\,{\rm cm}^{-2}, \qquad (10)$$

where the opacity at 353 GHz, τ_{353}, is taken from Planck Collaboration XI (2014). The conversion factor to the hydrogen column density, $N_{\rm H}$, is the value measured from the comparison with H I data at high Galactic latitudes (Planck Collaboration Int. XVII 2014; Planck Collaboration XI 2014). Going from high to intermediate Galactic latitudes we ignore the decrease in the ratio between $N_{\rm H}$ and τ_{353} by a factor of ~ 2 for increasing column densities, reported in Planck Collaboration XI (2014). Figure 6 presents the DF of $\Delta N_{\rm H}$. The distribution covers two orders of magnitude, from 10^{20} to $10^{22}\,{\rm cm}^{-2}$, with a median value of $1.2\times10^{21}\,{\rm cm}^{-2}$.

In Fig. 7 we compare the DFs of the extinction A_V derived from τ_{353} for the ridges and all the pixels in the Chamaeleon complex. We use the relation $A_V = R_V\,E(B-V) = 1.49\times10^4\,R_V\,\tau_{353}$ from Planck Collaboration XI (2014) and $R_V = 3.1$ (Jones et al. 2011; Schlafly & Finkbeiner 2011; Mörtsell 2013). The figure shows that the selected pixels cover most of the range of A_V measured over the entire Chamaeleon complex, except the lowest values.

Here, we explain how we estimate the mean gas density of the ridges using the curvature map. On the crest of a ridge, the first derivatives of the sky brightness with respect to Galactic coordinates are zero. The second derivative in the direction perpendicular to the ridge is λ_-. Along this direction, the local variation of the brightness over an angular distance ϵ may be approximated by a second-order Taylor expansion as

$$\delta D_{353} \approx 0.5|\lambda_-|\epsilon^2. \qquad (11)$$

The Hessian algorithm tends to select ridges with a thickness close to the $20'$ angular distance over which the derivatives of D_{353} are computed (Appendix A). Since this angular distance is barely larger than the angular resolution of the map ($15'$), the width of some of the structures that we analyse is not resolved in the smoothed D_{353} map. For all the selected structures we compute δD_{353} for $\epsilon = 20'$. The physical thickness in parsecs corresponding to ϵ is $\delta \approx \epsilon\,d$, where d is the distance to the ridges. We estimate the distance from the scale height of the H I emission of the cold neutral medium (CNM) in the solar neighbourhood, h, as $d = h/|\sin b|$. For $h = 100$ pc (see Fig. 14 in Kalberla et al. 2007), we find a mean distance over the latitudes of the selected pixels of $\bar{d} = 430$ pc, and a mean thickness of $\bar{\delta} = 2.5$ pc.

To estimate the mean gas density we first convert the brightness variation δD_{353} into column density variation

$$\delta N_{\rm H} = \frac{\delta D_{353}}{D_{353}} N_{\rm H}. \qquad (12)$$

Provided that the extent of the ridges along the line of sight is, on average, comparable to their thickness in the sky (δ), the mean density may be expressed as

$$\langle n_{\rm H}\rangle = \left\langle \frac{\delta N_{\rm H}}{\delta} \right\rangle, \qquad (13)$$

where the mean, $\langle\,...\,\rangle$, is computed over the selected pixels. We find $\langle n_{\rm H}\rangle = 300\,{\rm cm}^{-3}$, a value within the range of CNM gas densities. This conclusion is true even if the extent of the ridges along the line of sight is larger than their thickness in the sky. We stress that the value of $\langle n_{\rm H}\rangle$ only provides a rough estimate of the mean volume density, which we use to show that we are selecting CNM structures.

We have visually compared our map of ridges with the southern sky of the GASS survey (Kalberla et al. 2010) and we notice that many of the selected structures are also seen in H I but their column densities, and our density estimate, are high enough that a significant fraction of the gas must be molecular (Planck Collaboration XIX 2011; Planck Collaboration XXIV 2011; Wolfire et al. 2010), even if many of the selected ridges do not have a counterpart in CO maps (Dame et al. 2001; Planck Collaboration XIII 2014).

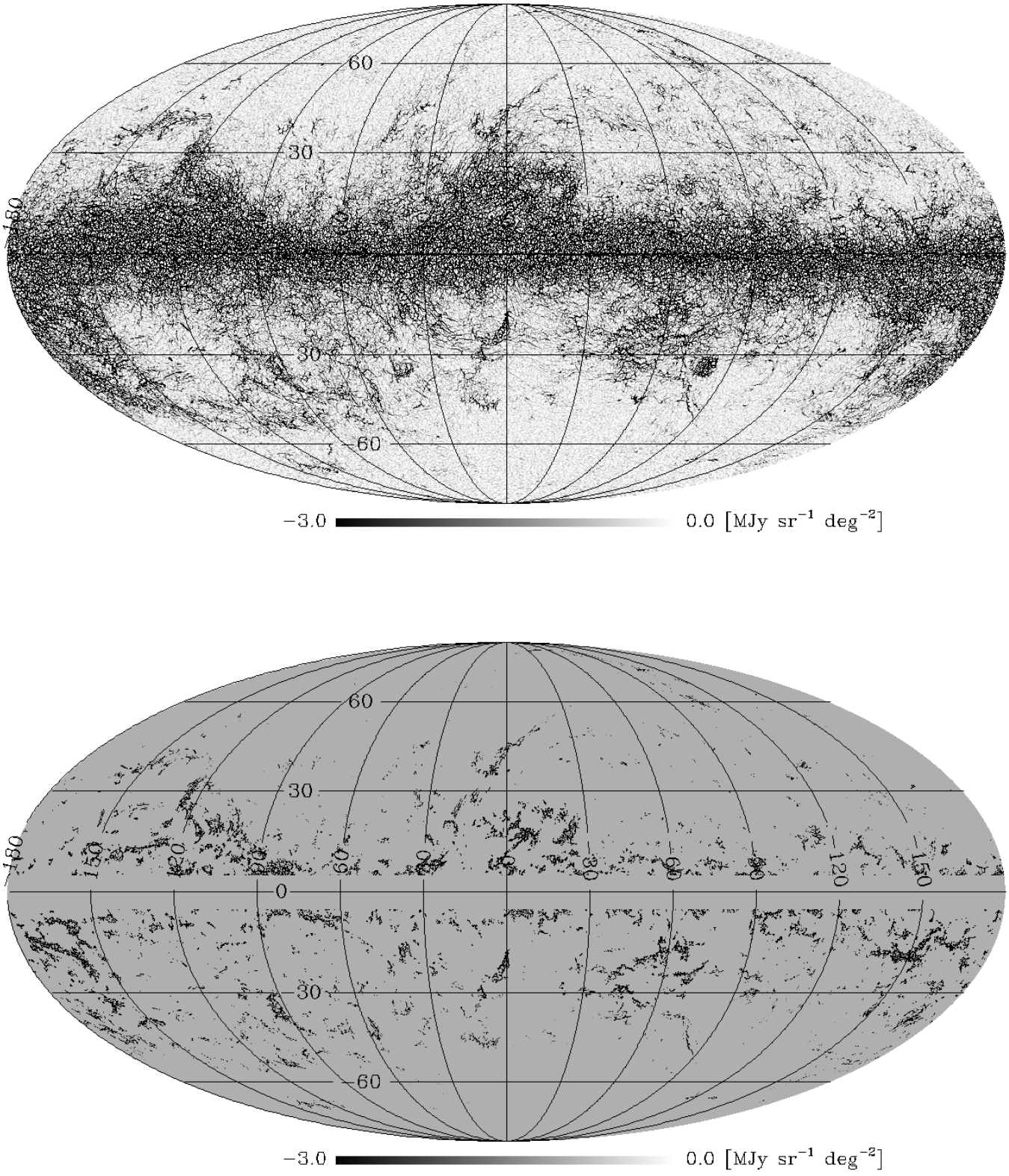

Fig. 3. *Top:* all-sky map of the negative curvature, λ_-, of D_{353}. *Bottom:* same as in the top panel where only the selected pixels are shown (see Sect. 4.2).

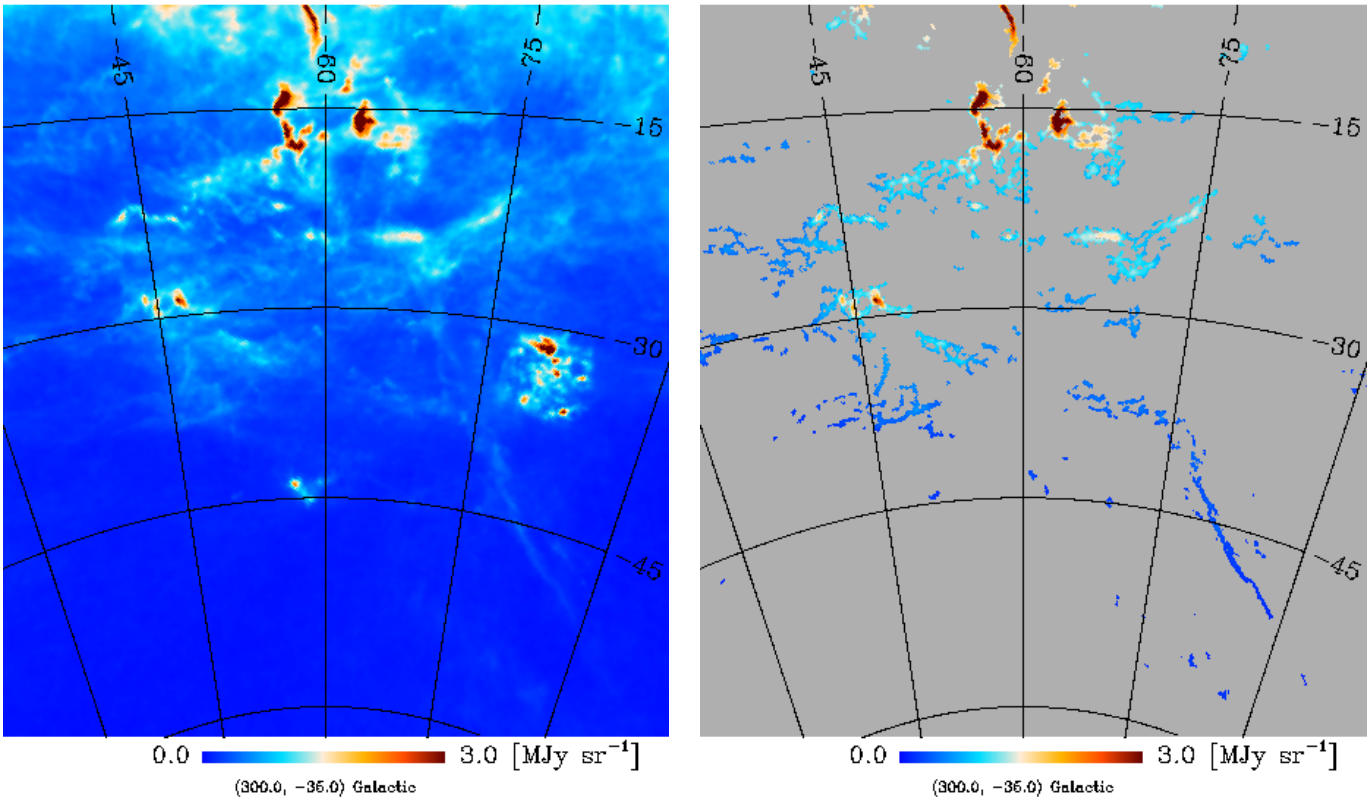

Fig. 4. *Left:* expanded view of the Chamaeleon complex in D_{353}. The centre of the map is at $(l, b) = (300°, -35°)$. *Right:* same as for the left panel with the masked pixels in grey. The Magellanic Clouds are masked.

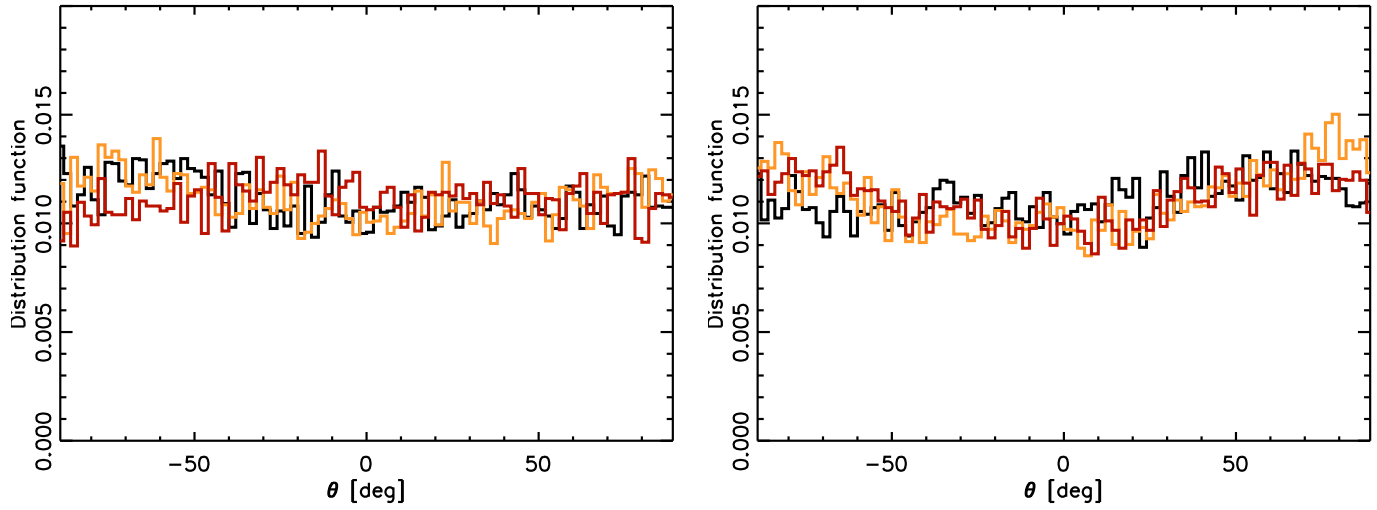

Fig. 5. *Left:* distribution functions of the orientation angle θ from Eq. (9) for the northern Galactic hemisphere and for 3 mean values of the Galactic latitude: $b = 7°$ (black curve), 15° (orange curve) and 33° (red curve). *Right:* same as for the left panel but for the southern hemisphere. The mean values of b are $-8°$ (black curve), $-20°$ (orange curve) and $-39°$ (red curve).

5. The dispersion of magnetic field orientations

The orientation of the magnetic field in interstellar clouds has often been inferred from the polarization of starlight occurring in the environment around the clouds, e.g. Li et al. (2013) for molecular clouds and Clark et al. (2014) for the diffuse ISM. The *Planck* maps allow us to compare the polarization angles on the filamentary ridges with those measured on the nearby back-

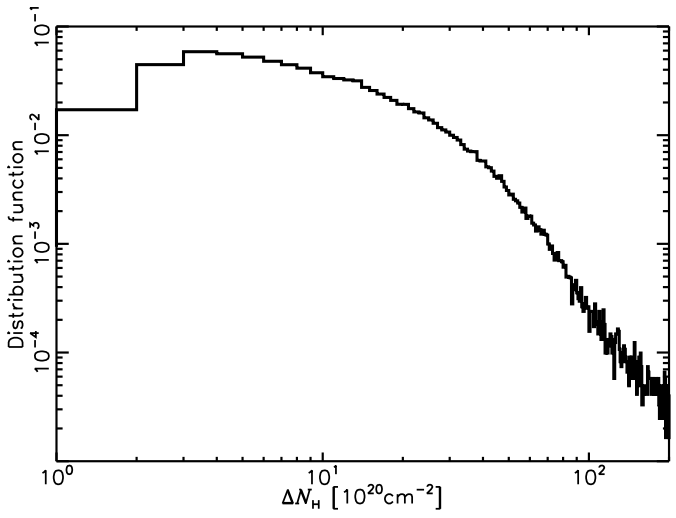

Fig. 6. Distribution function of the excess column density, $\Delta N_{\rm H}$ in Eq. (10), computed for the selected pixels.

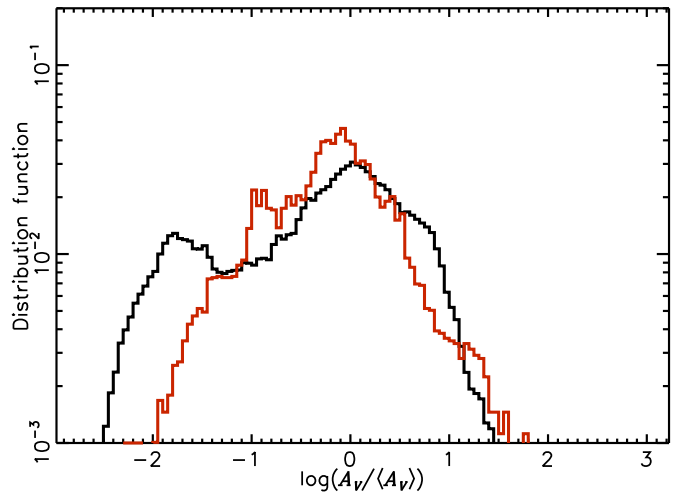

Fig. 7. Distribution functions of the extinction within the Chamaeleon complex. Here, $\langle A_V \rangle$ is the mean value of extinction over the whole Chamaeleon field. The figure shows the comparison between the DF of the total field (black line) and that relative to the selected pixels (red line). In both cases the Magellanic clouds are discarded.

ground. We present the DF of the difference of polarization angles in Sect. 5.1, and its modelling in Sect. 5.2 to estimate the ratio between the random and mean components of the magnetic field.

5.1. Difference between local and background polarization angles

We compute the polarization angles, for the ridges and the background, making use of $Q_{353}^{\rm Dif}$, $U_{353}^{\rm Dif}$ and $Q_{353}^{\rm BG}$, $U_{353}^{\rm BG}$, respectively. Inverting Eq. (1), we obtain

$$\psi_{353}^{\rm Dif} = \frac{1}{2}\tan^{-1}(U_{353}^{\rm Dif}, Q_{353}^{\rm Dif}),$$
$$\psi_{353}^{\rm BG} = \frac{1}{2}\tan^{-1}(U_{353}^{\rm BG}, Q_{353}^{\rm BG}). \quad (14)$$

The difference between the two polarization angles in Eq. (14), accounting for the 180° degeneracy that characterizes both, can be expressed as

$$\delta\psi = \frac{1}{2}\tan^{-1}\left(\frac{\sin 2\alpha \cos 2\beta - \cos 2\alpha \sin 2\beta}{\cos 2\alpha \cos 2\beta + \sin 2\alpha \sin 2\beta}\right), \quad (15)$$

where $\alpha = \psi_{353}^{\rm Dif}$, $\beta = \psi_{353}^{\rm BG}$. The values of $\delta\psi$ are computed from −180° to 180° matching both the sine and the cosine values.

The DF of $\delta\psi$ is presented in Fig. 8. On the plane of the sky, the magnetic field orientation is perpendicular to the polarization angle. Thus, the DF of $\delta\psi$ characterizes the difference between the magnetic field orientations determined at two different scales: that of the ridges, at 15′ (2 pc at the mean distance of 430 pc), and that of the local background, at 5° (40 pc). The DF of $\delta\psi$ has a mean value of 0° and a standard deviation of 40°, much larger than what we expect from data noise (Sect. 4.2). Thus, we conclude that the magnetic field on the ridges is statistically aligned with the background field, but with a significant scatter.

We check that the DF of $\delta\psi$ does not depend on the method we used to compute the background maps. For our selection of pixels, the polarization angle, $\psi_{353}^{\rm Dif}$, is close to ψ_{353}, the polarization angle at 353 GHz without background subtraction, computed with Q_{353} and U_{353} in Eq. (14). The DF of the difference between these two polarization angles, $\delta\psi_{\rm str}$, computed with Eq. (15) where $\alpha = \psi_{353}^{\rm Dif}$ and $\beta = \psi_{353}$, is shown in Fig. 9. This distribution has a standard deviation of 15°, which is smaller than that measured for $\delta\psi$. This result follows from the fact that, on the selected ridges, the local structures have statistically a dominant contribution to the values of the Stokes Q_{353} and U_{353} parameters. We also compute the same DF varying the percentage of pixels used to estimate the background maps (Sect. 3.2) from 20 % to 10 % and 40 %. The three DFs of $\delta\psi_{\rm str}$ are compared in Fig. 9. They are identical and much narrower than the DF of $\delta\psi$ in Fig. 8.

5.2. Modelling of the distribution function

We present a model, detailed in Appendix B, which takes into account the projection onto the plane of the sky and relates the width of the DF of $\delta\psi$ to the ratio between the random and mean components of the magnetic field.

The model is built from 3D vectors $\boldsymbol{V}_{\rm M}$ (hereafter, the subscript M refers to the model) with a Gaussian distribution of orientations about a mean reference vector, $\boldsymbol{V}_{\rm M0}$. Each component of $\boldsymbol{V}_{\rm M}$ is an independent realization of a Gaussian field on the sphere, with an angular power spectrum equal to a power law of index $\alpha_{\rm M} = -1.5$, to which we add the corresponding component of $\boldsymbol{V}_{\rm M0}$. By construction, the mean of $\boldsymbol{V}_{\rm M}$ is $\boldsymbol{V}_{\rm M0}$. The spectral index of the power spectrum allows us to introduce fluctuations about the mean direction correlated across the sky. This stochastic description of the field follows the early models proposed by Jokipii & Parker (1969). The degree of alignment between $\boldsymbol{V}_{\rm M}$ and $\boldsymbol{V}_{\rm M0}$ is parametrized by $f_{\rm M}$, the standard deviation of the modulus of the random component of $\boldsymbol{V}_{\rm M}$ normalized by $|\boldsymbol{V}_{\rm M0}|$. The DF of the angles between $\boldsymbol{V}_{\rm M}$ and $\boldsymbol{V}_{\rm M0}$ in 3D, per unit solid angle, is close to Gaussian with a standard deviation, $\sigma_{\rm M}$,

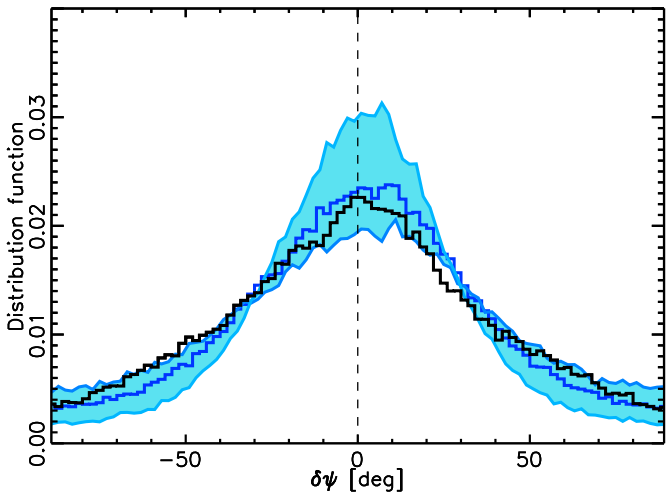

Fig. 8. Distribution function of $\delta\psi$, the difference between the polarization angle with background subtraction $\psi_{353}^{\rm Dif}$ and that of the background $\psi_{353}^{\rm BG}$, in black. The data are compared with Gaussian models computed for $f_{\rm M} \in [0.6, 1.0]$ in the light-blue band. The blue solid line represents the Gaussian model for $f_{\rm M} = 0.8$. The model parameter $f_{\rm M}$ measures the ratio between the strengths of the turbulent and mean components of the magnetic field.

which increases with $f_{\rm M}$. The models quantify statistically the projection of the 3D direction of the magnetic field onto the 2D celestial sphere. They do not include any averaging due to the superposition of uncorrelated structures along the line of sight, as done by Jones (1989) and Myers & Goodman (1991) for the modelling of polarization data towards the Galactic plane and molecular clouds.

For each model, we compute the projections of $\boldsymbol{V}_{\rm M}$ and $\boldsymbol{V}_{\rm M0}$ on the sky and the angle maps $\psi_{\rm M}$ and $\psi_{\rm M0}$ with respect to the local direction of the north Galactic pole. We use Eq. (15) with $\alpha = \psi_{\rm M}$ and $\beta = \psi_{\rm M0}$ to compute the difference, $\delta\psi_{\rm M}$, between these two angle maps. In Fig. 8, we show the DFs of $\delta\psi_{\rm M}$ for $f_{\rm M} \in [0.6, 1.0]$ as well as the model with $f_{\rm M} = 0.8$ that best matches the data. This value agrees with that inferred from the modelling of near-IR stellar polarization in the Galactic plane and molecular clouds by Jones (1989); Jones et al. (1992), and from synchrotron observations (Beck 2007; Houde et al. 2013; Haverkorn 2015). The comparison between the models and the data provides an estimate of the ratio between the amplitudes of the random (turbulent) and mean components of the magnetic field. The analogy with the data is such that $\psi_{353}^{\rm Dif}$ corresponds to the turbulent component of the field at 20′ scale, and $\psi_{353}^{\rm BG}$ to the mean component at a few degrees scale, on the sky.

This method is similar to the one proposed by Hildebrand et al. (2009) to measure the local difference of polarization angles in molecular clouds in order to separate the mean and turbulent components of the magnetic field. However, there are two main differences with what is described by this earlier work. First, we do not compute, nor fit, the dependence of the variance of the angle difference on the angular distance. Second, by measuring the dispersion of polarization angles over the whole sky, and by comparing the data with the Gaussian models, we obtain a 3D estimate of the ratio between the turbulent and mean components of the field, corrected for the projection of the magnetic field on the plane of the sky.

Equipartition between kinetic energy from turbulence and magnetic energy is found in the diffuse ISM from Zeeman H I observations, which implies that turbulence in the CNM is trans-Alfvénic (Myers et al. 1995; Heiles & Troland 2005).

Thus, our result fits with the Chandrasekhar and Fermi description of turbulence in the diffuse and magnetized ISM in terms of Alfvén waves(Chandrasekhar & Fermi 1953; Ostriker et al. 2001; Hildebrand et al. 2009). This framework assumes energy equipartition between the kinetic energy of the gas and the energy of the random component of the magnetic field. Our analysis suggests that this non-trivial assumption applies in the diffuse ISM.

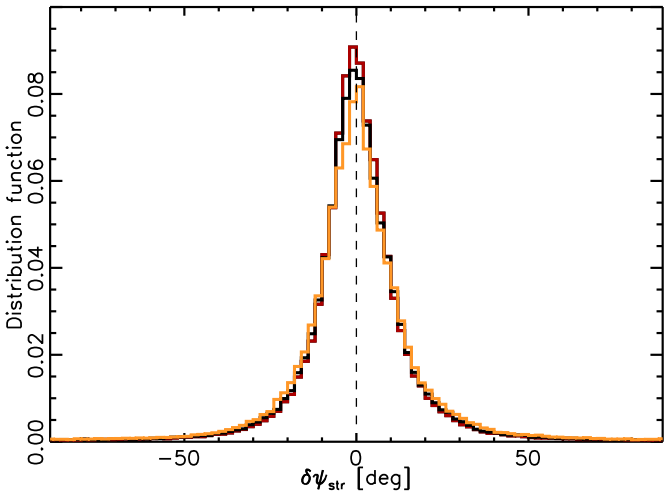

Fig. 9. Distribution function of $\delta\psi_{\rm str}$, the difference between the polarization angles with and without background subtraction, $\psi_{353}^{\rm Dif}$ and ψ_{353} respectively, computed over the selected pixels. The three curves show the DFs when we compute the local background among the 10 (red), 20 (black), and 40 % (orange) lowest values of D_{353} (see Sect. 3.2).

6. Alignment of the magnetic field and the matter structures in the diffuse ISM

We quantify the relative orientation between the magnetic field and ridges in the dust emission map. We present and discuss the statistical results from our data analysis in light of the Gaussian model in Appendix B, which takes into account projection effects. The global statistics presented in this section refer to the diffuse ISM because only a small fraction of the selected structures are within molecular clouds.

6.1. The alignment between the magnetic field and the matter structures

In order to calculate the relative orientation between the magnetic field and the ridges, we make a pixel-by-pixel comparison of the polarization angle ψ and the orientation angle θ of the ridges. We compute the difference, Θ, between the orientation of the ridge and that of the magnetic field inferred from the polarization angle, using Eq. (15) with $\alpha = \psi - 90°$ and $\beta = \theta$. In

Fig. 10, we show the DFs of Θ for the selected pixels, computed with $\psi = \psi_{353}^{\rm Dif}$, ψ_{353}, and $\psi_{353}^{\rm BG}$.

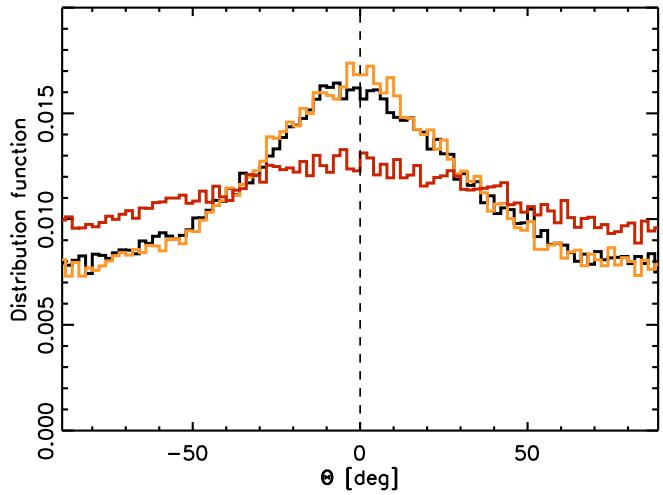

Fig. 10. Distribution function of Θ, the difference between the inferred orientation angle of the magnetic field and that of the ridges, for the selected pixels. The orange line and the black line represent the *Planck* data with ($\psi_{353}^{\rm Dif}$) and without (ψ_{353}) background subtraction, respectively. The red line refers to the polarization angle of the subtracted background ($\psi_{353}^{\rm BG}$). The structures of matter appear as statistically aligned with the orientation of the magnetic field projected on the plane of the sky.

A preferred alignment is observed for the two DFs computed with $\psi_{353}^{\rm Dif}$ and ψ_{353}, while that computed with $\psi_{353}^{\rm BG}$ is much broader. The comparison of the DFs in Fig. 10 leads to two main conclusions. First, the similarity between the DFs computed with and without background subtraction tells us that the background subtraction is not a critical aspect of our data analysis. This follows from the fact that, for the selected pixels, the polarized signal is dominated by the contribution of the ridges. Second, the fact that the DF obtained when comparing θ with $\psi_{353}^{\rm BG}$ is almost flat indicates that the matter structures are preferentially aligned with the local magnetic field, rather than with the background field.

6.2. Correlation between alignment and polarization fraction

In spite of the predominant alignment of the interstellar matter structures with the magnetic field, all DFs in Fig. 10 show a broad dispersion, with a significant probability up to 90° from the central peak. The widths of the DFs are much larger than those computed for the uncertainty in the polarization angle, and in the direction of the ridges in Appendix A.

The DFs of Θ combine the intrinsic scatter in the relative orientations between the matter structures and the magnetic field in 3D with the projection onto the plane of the sky. Thus, we expect the shape of the DF to depend on the orientation of the magnetic field with respect to the line of sight. Where the magnetic field orientation is close to the line of sight, the polarization angle on the plane of the sky does not strongly constrain the orientation of the field and, thereby, its relative orientation with the ridges in the dust map.

The analysis of the polarization maps, built from the 3D MHD simulation in Planck Collaboration Int. XX (2014), shows that the polarization fraction p in Eq. (3) traces $\cos^2\gamma$ averaged over the line of sight (see their Fig. 21). Although p also depends on changes of the magnetic field orientation along the line of sight (Planck Collaboration Int. XIX 2014; Planck Collaboration Int. XX 2014), depolarization along the line of sight and within the beam does not preclude the use of p to statistically test the impact of projection effects on the DF of Θ. We do find that the relative orientation between the matter structures and the magnetic field depends on p. In Fig. 11, we compare the DFs computed with $\psi_{353}^{\rm Dif}$ for all the selected ridges, for those with the 30 % highest values of p and for the lowest 30 %. The higher the polarization fraction, the sharper the peak at 0° of the DF of Θ.

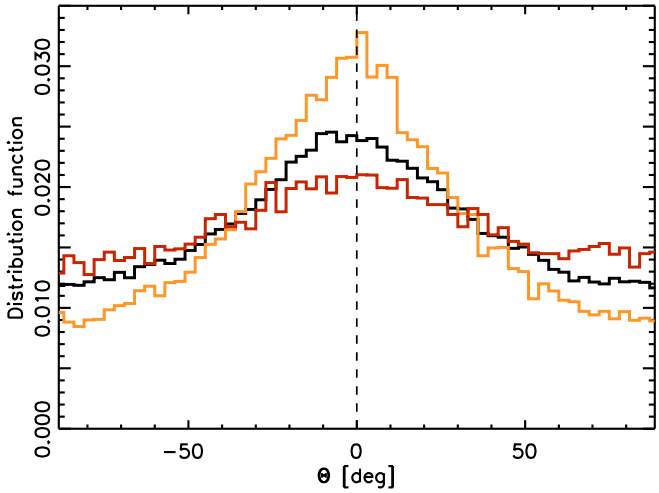

Fig. 11. Distribution function of Θ computed with $\psi_{353}^{\rm Dif}$ as a function of the polarization fraction p of the selected structures. The black line represents all the selected pixels. The orange line refers to the pixels with the 30 % highest values of p and the red line to the 30 % lowest. The distribution of relative orientations is the sharpest for the highest values of p.

To quantify the projection effects on the relative orientation, we make use of the model presented in Sect. 5 and Appendix B. Here, we make the assumption that the magnetic field can be decomposed into a component aligned with the orientation of the ridges and a random component with zero mean. In the model, the orientation of the ridges is fixed to the constant vector $\boldsymbol{V}_{\rm M0}$. The degree of alignment between the field and the ridges is parametrized by $\sigma_{\rm M}$ the standard deviation of the DF per unit solid angle of the angle between $\boldsymbol{V}_{\rm M}$ and $\boldsymbol{V}_{\rm M0}$. As an example, Fig. 12 shows the DFs of the angle differences between the projection onto the plane of the sky of $\boldsymbol{V}_{\rm M}$ ($\psi_{\rm M}$) and $\boldsymbol{V}_{\rm M0}$ ($\psi_{\rm M0}$) for $\sigma_{\rm M} = 33°$. The plot compares the relative orientations for all the selected pixels and for those with the 30 % highest and lowest values of $\cos^2\gamma_{\rm M}$, hereafter the projection factor, where $\gamma_{\rm M}$ is the angle between $\boldsymbol{V}_{\rm M}$ and the plane of the sky. These three DFs compare well with those of Θ in Fig. 11. The Gaussian model, which takes into account projection effects, reproduces the main characteristics of the DFs computed on the data, including the dependence on the polarization fraction. The data and the model are further compared in the next section.

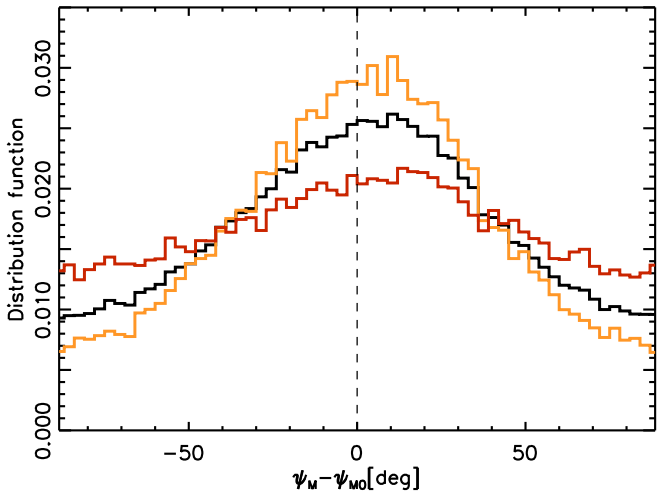

Fig. 12. Distribution functions of relative orientations between $\boldsymbol{V}_{\rm M}$ and $\boldsymbol{V}_{\rm M0}$ for the Gaussian model described in the text and Appendix B for $\sigma_{\rm M} = 33°$. For the model, the polarization fraction is the projection factor $\cos^2\gamma_{\rm M}$. We use for the models the same mask as for the data. The black line represents all the selected pixels. The orange (red) line refers to the structures with the 30 % highest (lowest) values of $\cos^2\gamma_{\rm M}$. This figure shows that projection effects may reproduce the same trends found for the data.

6.3. The ξ parameter: the degree of alignment

To quantify the variation of the DF of Θ, $H(\Theta)$, with the polarization fraction, we introduce a normalized version of the parameter used by Soler et al. (2013) to study the relative orientation between magnetic fields and density structures in MHD simulations. We compute an estimator of the probability of having Θ near 0° as

$$A_{\rm in} = \int_{-20°}^{20°} H(\Theta){\rm d}\Theta, \tag{16}$$

where the subscript 'in' stands for inner range, and near ±90° as

$$A_{\rm out} = \int_{-90°}^{-70°} H(\Theta){\rm d}\Theta + \int_{70°}^{90°} H(\Theta){\rm d}\Theta, \tag{17}$$

where the subscript 'out' stands for outer range. We define the degree of alignment ξ as

$$\xi = \frac{A_{\rm in} - A_{\rm out}}{A_{\rm in} + A_{\rm out}}. \tag{18}$$

The ξ parameter spans values between −1 and 1, depending on whether the DF peaks in the outer or inner range of angles, respectively.

In Fig. 13, we study the dependence of ξ on p by binning the latter and keeping a constant number of pixels in each bin. For each bin of p, we compute $H(\Theta)$ and ξ and we find that, on the sky, ξ increases with p. We check that this dependence is not affected by noise. Using the error map from Planck Collaboration Int. XIX (2014), we compute a Gaussian realization of the noise in the polarization angle that we add to the data to increase the noise level by a factor of $\sqrt{2}$. We find that the dependence of ξ on p, obtained for the noisier angle map, is the same as that in Fig. 13.

In Fig. 13, the data are compared with model results that show how ξ varies with $\cos^2\gamma_{\rm M}$ for increasing values of $\sigma_{\rm M}$. We find that ξ correlates with the projection factor. The model that best matches the data has $\sigma_{\rm M} = 33°$. This value of $\sigma_{\rm M}$ corresponds to a preferred alignment, where the angle between matter structures and the magnetic field in 3D is within 45° for about 80 % of the selected ridges.

For the data, unlike for the Gaussian model where $p = \cos^2\gamma_{\rm M}$, the polarization fraction depends on the line-of-sight depolarization. Depolarization results from the dispersion of the magnetic field orientation along the line of sight, and within the beam (Fiege & Pudritz 2000). Planck Collaboration Int. XIX (2014) used maps of the dispersion of the polarization angle, $\mathcal{S}$, to quantify local variations of the magnetic field orientation. They defined $\mathcal{S}$ as

$$\mathcal{S}(\boldsymbol{x},\delta) = \sqrt{\frac{1}{N}\sum_{i=1}^{N}[\psi(\boldsymbol{x}) - \psi(\boldsymbol{x}+\boldsymbol{\delta_i})]^2}, \tag{19}$$

where $|\boldsymbol{\delta_i}| = \delta$. Planck Collaboration Int. XIX (2014) report a general trend where the regions in the sky with high (low) values of $\mathcal{S}$ have low (high) polarization fraction; the fractional variation of $\mathcal{S}$ is equal to that of p. $\mathcal{S}$ is an indicator of the depolarization along the line of sight associated with the tangling of the field within the beam. This interpretation is supported by Planck Collaboration Int. XX (2014), who point out that $\mathcal{S}$, computed from their 3D MHD simulation, does not vary with the mean projection factor for $\mathcal{S} > 5°$ (see their Fig. 24). In Fig. 14, we plot ξ as a function of $\mathcal{S}$ computed on the data using the same binning procedure applied for p. We find a slight decrease in ξ versus $\mathcal{S}$ much smaller than the increase in ξ versus p. This result supports our interpretation of the dependence of ξ on p, which results primarily from the orientation of the field with respect to the plane of the sky.

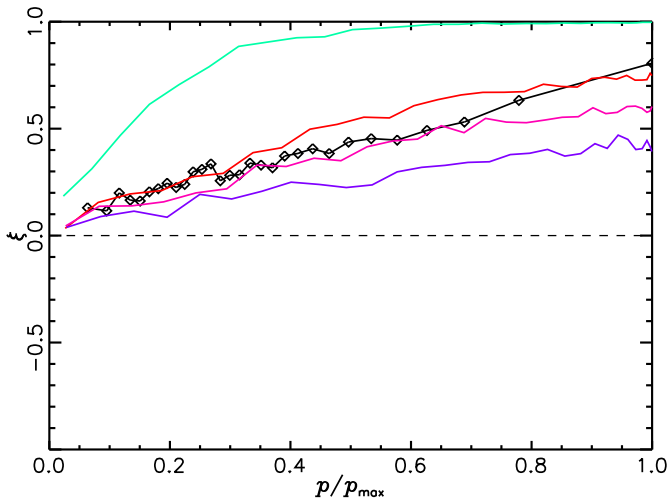

Fig. 13. Correlation between the degree of alignment, ξ, and the polarization fraction, p, for the selected pixels, both for data (black squares) and for the Gaussian models. The models are characterized by the following values of $\sigma_{\rm M}$: 15° in green, 29° in red, 33° in magenta and 38° in purple. The data values of p are normalized to the maximum value, $p_{\rm max}$, within the sample. For the models, $p = \cos^2\gamma_{\rm M}$. This figure shows that projection effects, probed by the Gaussian models, are likely to be the main cause of the correlation between ξ and p.

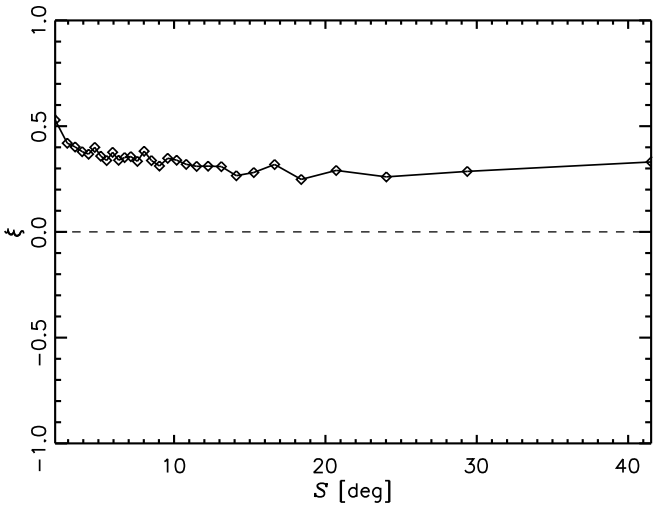

Fig. 14. Dependence of the degree of alignment, ξ, on $\mathcal{S}$, the local dispersion of the polarization angle, an empirical tracer of depolarization along the line of sight and within the beam. This plot shows that ξ does not significantly depend on $\mathcal{S}$.

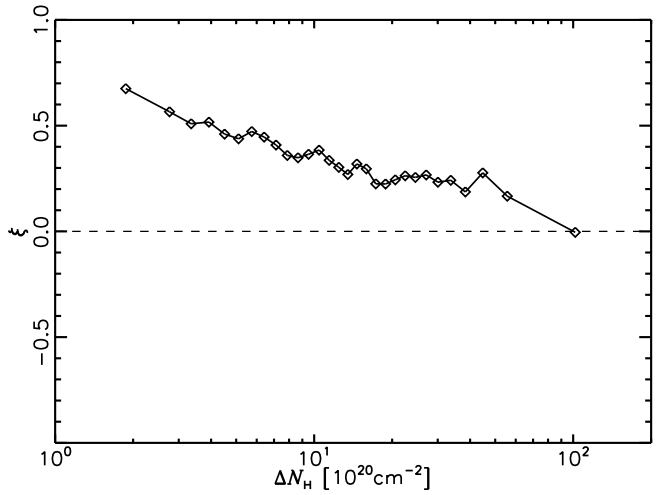

Fig. 15. Variation of the degree of alignment, ξ, as a function of the excess column density, $\Delta N_{\rm H}$, for the selected pixels. The degree of alignment decreases for increasing values of the column density.

7. Relative orientation between the magnetic field and the matter structures in molecular clouds

We extend our statistical analysis to molecular clouds characterizing how the degree of alignment between the matter structures and the magnetic field varies with column density. In Sect. 7.1, we show that the degree of alignment decreases for increasing column density. Maps of the relative orientation are presented for the Chamaeleon and Taurus molecular clouds in Sect. 7.2.

7.1. ξ versus $\Delta N_{\rm H}$ over the whole sky

We quantify the dependence of the degree of alignment ξ on the excess column density of the selected ridges $\Delta N_{\rm H}$ (see Sect. 4).

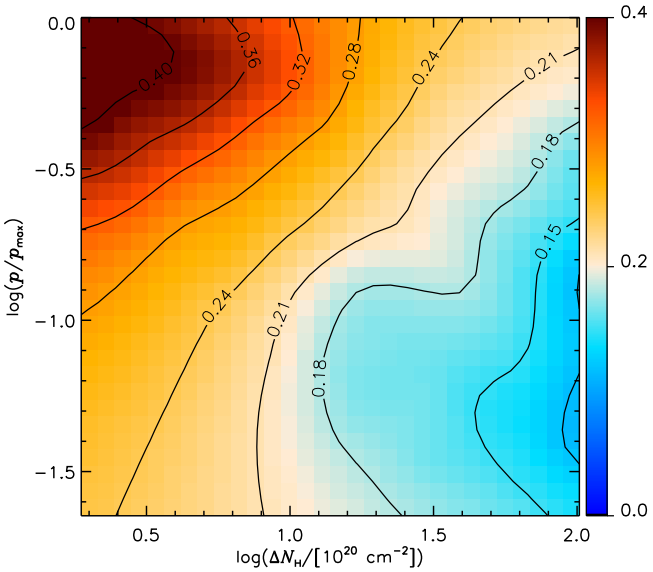

Fig. 16. Map and contours of the degree of alignment, ξ, as a function of p and $\Delta N_{\rm H}$. Only the selected pixels are taken into account for computing ξ. This figure shows that ξ depends on both quantities, p and $\Delta N_{\rm H}$.

We bin $\Delta N_{\rm H}$, applying the same binning procedure as for p. We find that ξ is anti-correlated with $\Delta N_{\rm H}$, as shown in Fig. 15.

The *Planck* polarization data show an overall anti-correlation between polarization fraction and column density (Planck Collaboration Int. XIX 2014; Planck Collaboration Int. XX 2014). We test that the decrease in ξ with $\Delta N_{\rm H}$ does not result from this variation of p with column density. In Fig. 16, we present a map that characterizes the variations of ξ both as a function of p and $\Delta N_{\rm H}$. We bin the selected pixels first in $\Delta N_{\rm H}$ and then in p, ensuring that we have the same number of elements for each bin of both variables. Given a 2D bin, we compute the corresponding $H(\Theta)$ and ξ. We then interpolate the ξ map over a regular grid of values for p and $\Delta N_{\rm H}$. The map of ξ confirms the decrease in alignment from low to high excess column densities and from high to low polarization fractions. The degree of alignment clearly depends on both p and $\Delta N_{\rm H}$.

7.2. A glimpse into molecular clouds

The anti-correlation found between ξ and $\Delta N_{\rm H}$ suggests that at high column densities, within molecular clouds, the degree of alignment between the magnetic fields and matter structures decreases. To discuss this result we present maps of the Taurus and the Chamaeleon molecular clouds, as representative examples of molecular complexes in the solar neighbourhood. For comparison, Fig. 18 illustrates two fields at intermediate Galactic latitudes, which sample the diffuse ISM.

The four panels in Figure 17 show the extinction maps derived from the dust sub-mm opacity in Planck Collaboration XI (2014) next to the corresponding maps of alignment quantified by $\cos 2\Theta$. The cosine function spans values between -1 and 1, identifying structures that are perpendicular and parallel to the magnetic field, respectively. We stress that the cosine representation, chosen for visualization, stretches the contrast of the Θ distribution towards the extrema. On the extinction maps, we plot the vectors tracing the magnetic field orientation inferred from $Q_{353}^{\rm Dif}$ and $U_{353}^{\rm Dif}$.

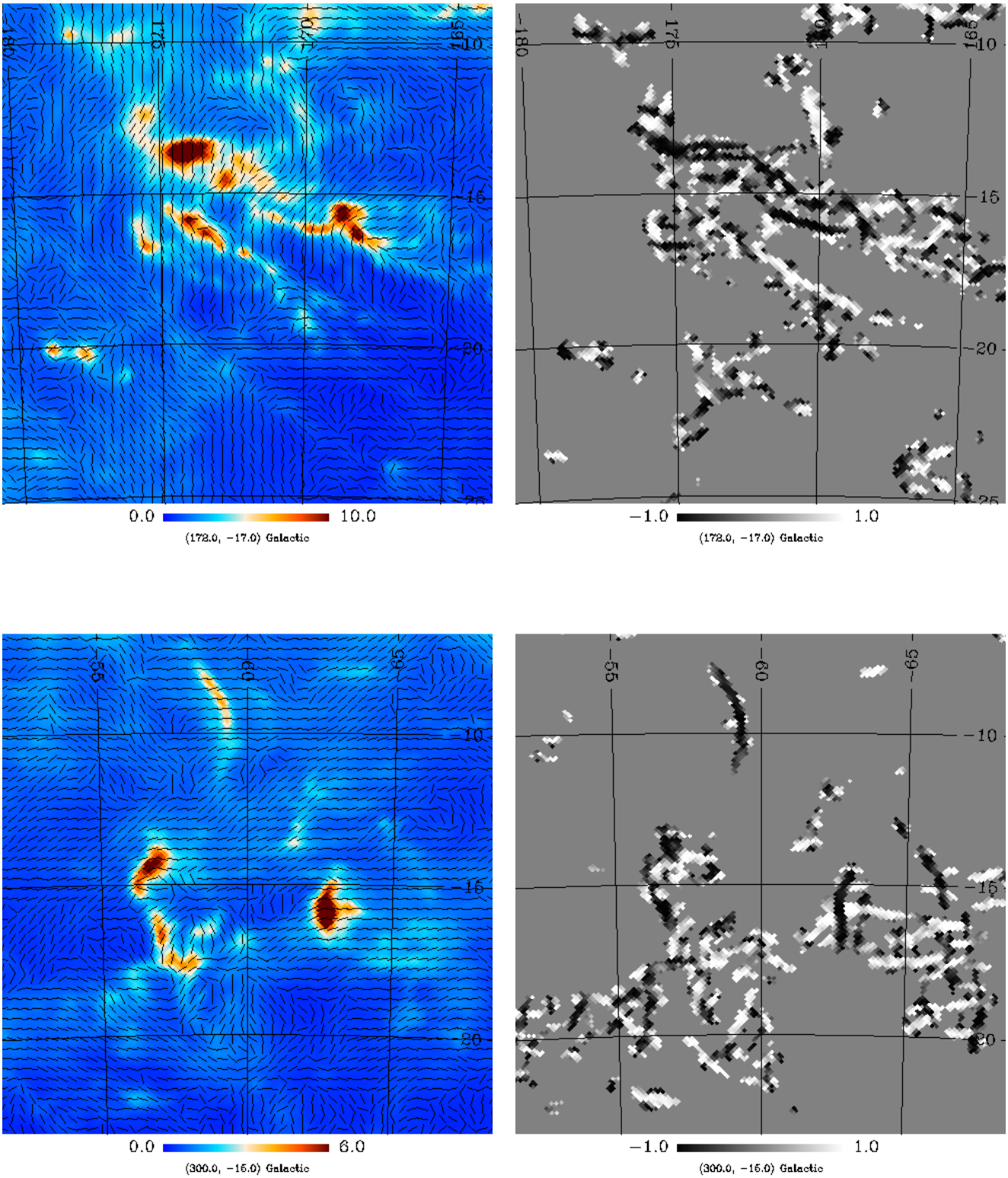

Fig. 17. *Left*: maps of the visual extinction A_V derived from the sub-mm dust opacity from Planck Collaboration XI (2014) at the 15′ resolution of our analysis for the Taurus molecular cloud (*top*), and the Chamaeleon molecular complex including the Musca filament (*bottom*). The vectors tracing the magnetic field orientation, computed from $Q_{353}^{\rm Dif}$ and $U_{353}^{\rm Dif}$, are plotted with a fixed length. *Right*: corresponding maps of the relative orientation between matter structures and magnetic field quantified by $\cos 2\Theta$ for the selected structures (Sect. 4). This figure shows coherent structures where the cosine is either positive or negative, corresponding to a magnetic field aligned with, or perpendicular to the structures.

The maps of relative orientation in the Taurus and Chamaeleon clouds (Fig. 17) reveal some coherent structures where the magnetic field tends to be perpendicular to the interstellar ridges, in particular to those with the highest extinction, while in the diffuse ISM (Fig. 18), in agreement with the DFs of Θ presented in Sect. 6.1, there is a predominance of structures parallel to the magnetic field. Hence, the flattening of $H(\Theta)$ as a function of $\Delta N_{\rm H}$ might be associated with the presence of matter structures that are perpendicular to, rather than aligned with, the magnetic field, and not related to a loss of correlation between the field and the structure of matter.

In Appendix B, we show maps of $\cos 2\Theta$ in Taurus and Chamaeleon computed with a Gaussian model where we set $\boldsymbol{V}_{\rm M0}$ to zero in order to quantify the effect of projection onto the plane of the sky when the orientations of the magnetic field and the matter structures are uncorrelated. The spectral index used in the Gaussian realizations, $\alpha_{\rm M} = -1.5$, introduces a correlation in the orientation of $\boldsymbol{V}_{\rm M}$ over the sky, which is independent of the structure of matter. The maps of $\cos 2\Theta$ computed with this model, shown in Fig. B.4, present small black or white structures that appear perpendicular or parallel with respect to the magnetic field orientation. However, prominent elongated features, with the magnetic field oriented preferentially orthogonal to the matter structures, seen in the sky images in Fig. 17, such as the Musca filament, are absent in the model images in Fig. B.4. This difference suggests that in molecular clouds there is a significant number of matter structures, which tend to be perpendicular to the magnetic field, explaining the decrease in ξ with $\Delta N_{\rm H}$.

Dust polarization in molecular clouds allows us to trace the field orientation in high column-density structures, as detailed in Planck Collaboration et al. (2014), where three examples are analysed. Thus, we consider it unlikely that the decrease in ξ with $\Delta N_{\rm H}$ is due to a loss of polarization from either enhanced turbulence or reduced dust grain alignment efficiency for increasing column density (Falceta-Gonçalves et al. 2008; Whittet et al. 2008; Jones et al. 2015). Furthermore, this alternative interpretation is not supported by the fact that ξ decreases for increasing $\Delta N_{\rm H}$, independently of its dependence on p (see Fig. 16).

The *Planck* images should not be interpreted, however, as evidence for two distinct orientations with respect to that of the magnetic field, with depletion at intermediate angles. Such a bimodality was suggested by previous studies based on extinction data for dark clouds (Li et al. 2013) and MHD simulations (Soler et al. 2013), but questioned by other observational studies (Goodman et al. 1990; Houde et al. 2004). Our all-sky analysis does not show a significant turn-over in the statistics of relative orientation between the matter structures and the magnetic field, from the diffuse ISM to molecular clouds.

Because of projection effects, it is difficult to identify a bimodal distribution between magnetic fields and matter structures in a statistical way. To quantify this statement, we introduce a bimodal configuration of relative orientations in 3D between $\boldsymbol{V}_{\rm M}$ and $\boldsymbol{V}_{\rm M0}$ in the Gaussian models (Appendix B) using a new model parameter η, which represents the fraction of sky pixels where $\boldsymbol{V}_{\rm M}$ is distributed about a second reference direction perpendicular to $\boldsymbol{V}_{\rm M0}$. Essentially, if η is the probability of having the mean of $\boldsymbol{V}_{\rm M}$ perpendicular to $\boldsymbol{V}_{\rm M0}$, then $1-\eta$ represents the probability of having the mean of $\boldsymbol{V}_{\rm M}$ parallel to $\boldsymbol{V}_{\rm M0}$. So far, throughout the paper, the models have been used with $\eta = 0$. The dispersion of the distribution of angles, $\sigma_{\rm M}$, is the same for both directions. In Fig. 19, we show the impact of the value of η on the DF of $\delta\psi_{\rm M}$, for $\sigma_{\rm M} = 33°$. Up to $\eta = 0.7$, the DF is nearly flat and does not indicate any turn-over in the relative orientations.

8. Discussion

This paper presents the first analysis across the whole sky comparing column density structures in the ISM with the orientation of the Galactic magnetic field. Previous studies focused on dark clouds (e.g. Goodman et al. 1995; Pereyra & Magalhães 2004; Alves et al. 2008; Chapman et al. 2011) where the magnetic field was found mainly, but not systematically, perpendicular to the long axis of the clouds. Our sample of ridges, built from the *Planck* dust map, is dominated by structures in the CNM of the diffuse ISM. For these structures we find a preferred alignment with the magnetic field projected on the plane of the sky. This trend disappears for the highest column densities in molecular clouds,where the data show coherent structures, which tend to be perpendicular to the magnetic field orientation.

In the next paragraphs, we discuss these observational results in light of models and MHD simulations, which attempt to describe the respective roles of the magnetic field, turbulence and the gas self-gravity in the formation of structures in the magnetized ISM.

The alignment between the magnetic field and matter structures in the diffuse ISM reported in Sect. 6 could be a signature of the formation of CNM filaments through turbulence. Their formation could be initiated by a local compression that would trigger the condensation of cold gas out of the warm neutral phase (Audit & Hennebelle 2005; Inoue & Inutsuka 2009; Heitsch et al. 2009; Saury et al. 2014). The shear of the turbulent flow would then stretch the gas condensations into structures, such as sheets and filaments, which would appear elongated in column density maps. These structures will tend to be aligned with the magnetic field if the gas velocity is dynamically aligned with the field (Brandenburg & Lazarian 2013). Furthermore, where the velocity shear stretches matter into filaments, the field is stretched in the same direction, creating alignment because the field is frozen into matter.[3] This interpretation was proposed by Hennebelle (2013) who found a strong correlation between the orientation of the density structures and that of the maximum shear of the velocity field in his MHD simulations. Although beyond the scope of this paper, from an observational point of view, the correlation between density structures and shear can be tested by looking for line-of-sight velocity gradients along filaments in H I and CO surveys. Where the filaments are inclined with respect to the plane of the sky, we can measure both the polarization angle and the radial component of the gas velocity.

For supersonic turbulence, gas sheets and filaments can also be formed by gas compression in shocks. For sub-Alfvénic turbulence (strong magnetic field with respect to turbulence), compression preferentially occurs where gas flows along the magnetic field lines, creating, thereby, structures perpendicular to the field. This cannot be the dominant process because we observe preferred alignment between matter structures and the magnetic field. For super-Alfvénic turbulence (weak magnetic field), gas compression also occurs for all directions of the shock velocity enhancing the component of the magnetic field perpendicular to the shock velocity, because of magnetic flux conservation and freezing into matter.[4] In this case, shocks tend to form structures aligned with the field.

For the highest column density ridges in molecular clouds, the interpretation must also involve self-gravity, which is known

[3] The formation of filaments by shear is illustrated in Fig. 3 of Hennebelle (2013).

[4] See Fig. 4 in Hartmann et al. (2001) for an illustration.

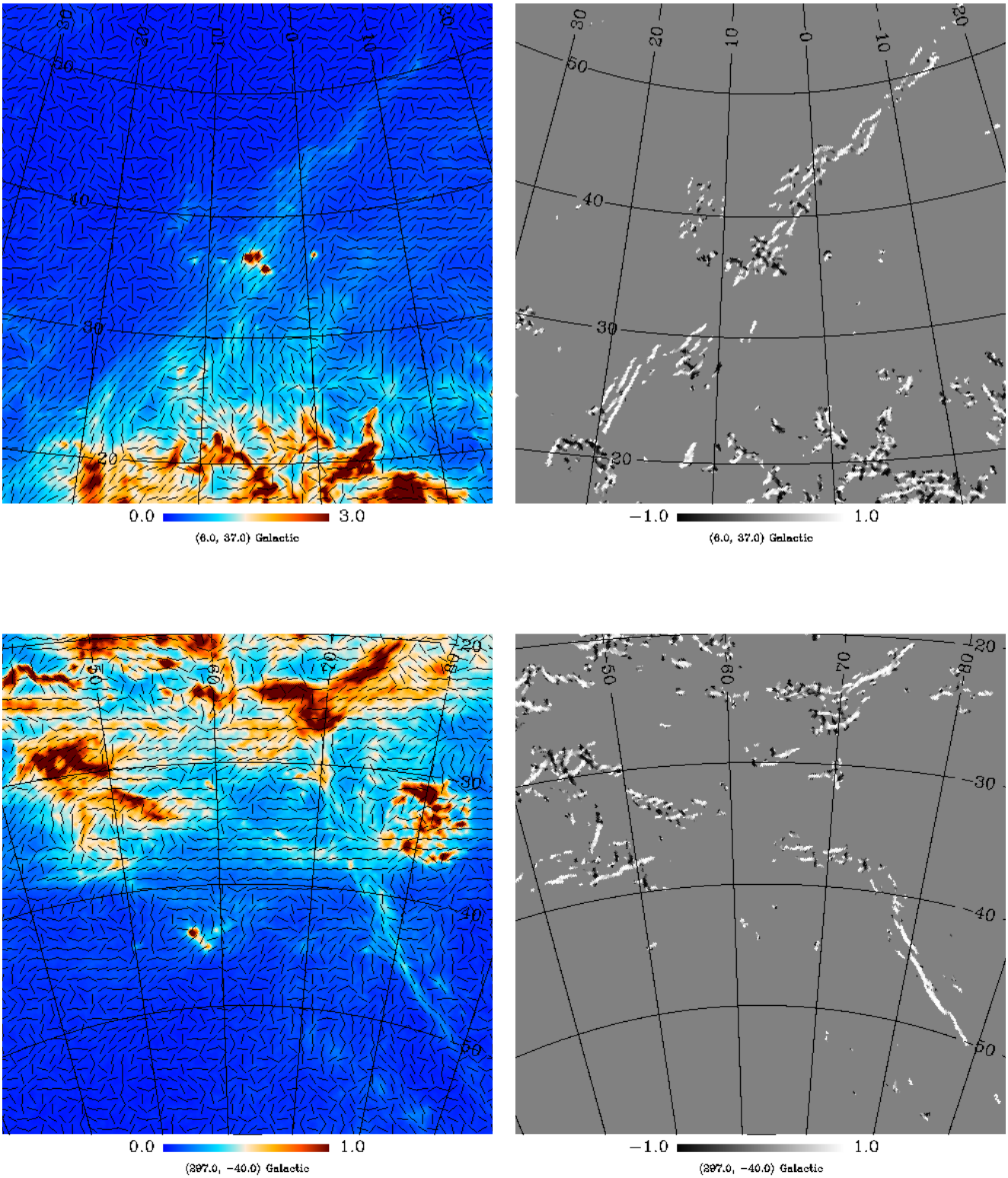

Fig. 18. Same as in Fig. 17 but for two fields at intermediate Galactic latitudes sampling the diffuse ISM. The central pixel for the top panels corresponds to (l, b)=(6°, 37°). The central pixel for the bottom panels corresponds to (l, b)=(295°, −40°). The Magellanic Clouds in the bottom extinction map (left) are masked. Most of the structures in the relative orientation maps appear as parallel to the magnetic field.

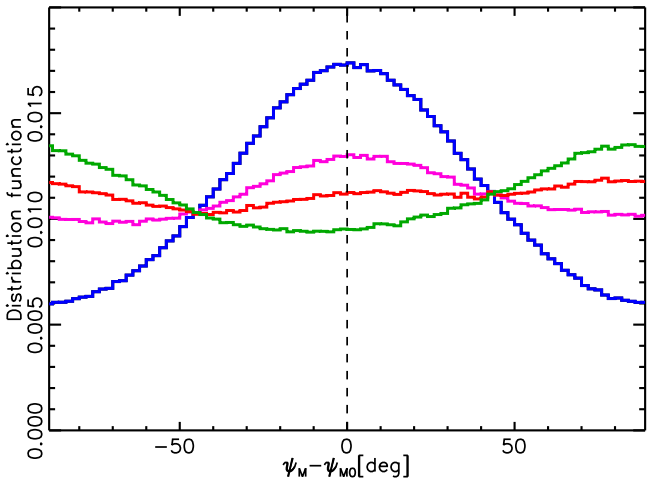

Fig. 19. Distribution functions of relative orientations for the Gaussian model with $\sigma_M = 33°$. The distributions show the effects of projection onto the plane of the sky of the 3D relative orientations between $\boldsymbol{V}_M$ and $\boldsymbol{V}_{M0}$. The curves refer to four different configurations depending on η, the fraction of 3D perpendicular orientations between the two vectors. For the blue curve, $\eta = 0$. For the pink, red, and green curves, η is 0.5, 0.7 and 0.9, respectively.

to amplify anisotropic structure (Lin et al. 1965). A gravitationally unstable cloud first collapses along the shortest dimension, forming a sheet, which subsequently breaks into elongated filamentary structures. The presence of a large-scale magnetic field can influence this effect, as the collapse can preferentially be along the mean field direction. Here, it is necessary to distinguish between sub-critical and super-critical structures (Mouschovias & Spitzer 1976). When a gravitationally bound structure forms, gravitational and turbulent energies are comparable and turbulence is sub-Alfvénic (super-Alfvénic) for sub-critical (super-critical) structures. For sub-critical structures, the magnetic field is dynamically important and gravity pulls matter preferentially along field lines. As a consequence, in sub-critical clouds gravitationally bound sheets and filaments are expected to be perpendicular to the magnetic field. The presence of striations orthogonal to the high column density filaments in *Herschel* maps of nearby molecular clouds, such as Taurus, supports this scenario (Palmeirim et al. 2013).

A bimodal distribution of orientations of structures with respect to the magnetic field is observed in numerical simulations. In their MHD simulations of molecular clouds, Soler et al. (2013) find a change in the relative orientation between matter structures and the magnetic field, from parallel to perpendicular, for gravitationally bound structures. This change is most significant for their simulation with the highest magnetization. We will need to combine our polarization data with velocity and column density measurements in order to test whether the perpendicularity between the magnetic field and the matter structures is a sign of filaments formed by self-gravity in magnetically dominated interstellar clouds.

9. Summary and perspectives

The *Planck* 353 GHz all-sky polarization maps provide unprecedented information, on the structure of the Galactic magnetic field and its correlation with interstellar matter.

Most of the structures (i.e. ridges) observed in the dust intensity map outside the Galactic plane are also seen as coherent structures in the dust Stokes Q and U maps. We performed a statistical analysis of the *Planck* data on these structures of matter, measuring their orientation from a Hessian analysis of the dust intensity map, and that of the magnetic field from the dust polarization. Our data analysis characterizes the variation of the magnetic field orientation between the structures and their local background, and the relative orientation between the structures and the magnetic field, with unprecedented statistics. Our sample of structures covers roughly 4 % of the sky and spans two orders of magnitude in column density from 10^{20} to 10^{22} cm^{-2}. In the following, we summarize the main results of our analysis.

We separated the polarized emission of the structures from that of the surrounding Galactic background within a few degrees on the sky. Comparing polarization angles, we estimate the ratio between the typical strengths of the turbulent and mean components of the field to be between 0.6 and 1.0, with a preferred value of 0.8. This result is in agreement with Zeeman H I observations indicating an approximate equipartition between turbulent and magnetic energies in the diffuse ISM.

We find that the interstellar matter structures are preferentially aligned with the magnetic field inferred from the polarization angle measured at the position of the structures. We introduced a parameter ξ that quantifies the degree of alignment between the orientation of the magnetic field and matter structures. We find that ξ increases with the polarization fraction p. We interpret this correlation in light of Gaussian models, which take into account the projection onto the plane of the sky of the 3D configuration between the magnetic field and the structures. Where the polarization fraction is low, the field tends to be close to the line of sight. In this configuration, the orientation of the magnetic field is not well constrained by the observations because its projection onto the plane of the sky is a minor component of the field. This geometric interpretation of the correlation between ξ and p is supported by the weakness of the dependence of ξ on the local dispersion of the polarization angle. The Gaussian models best match the data for a standard deviation between the orientation of the magnetic field and that of the structures of matter of 33° in 3D.

We find that ξ decreases for increasing column density, and that there is no alignment for the highest column density. This result does not reflect an absence of correlation between the structures of matter and the magnetic field, at high N_H. Structures that tend to be perpendicular to the magnetic field appear in molecular clouds, where they contribute to the statistics of relative orientations. We show maps of the Taurus and the Chamaeleon molecular complexes that support this interpretation.

We have presented the first analysis on the relative orientation between the filamentary density structures of the ISM and the Galactic magnetic field across the whole sky. The main outcome of this study is that, at the angular scales probed by *Planck*, the field geometry, projected on the plane of the sky, is correlated with the distribution of matter in the solar neighbourhood. In the diffuse ISM, the structures of matter are preferentially aligned with the magnetic field, while perpendicular structures appear in molecular clouds.

Our results support a scenario of formation of structures in the ISM where turbulence organizes matter parallel to the mag-

netic field in the diffuse medium, and the gas self-gravity produces perpendicular structures in the densest and magnetically dominated regions. This tentative interpretation on the role of turbulence in structuring interstellar matter may be tested by comparing the relative orientation of structures and the magnetic field with line-of-sight velocity gradients. It will also be interesting to apply our statistical analysis to MHD simulations of the diffuse ISM. Statistical analysis also needs to be complemented by detailed studies of specific structures in the diffuse ISM and in molecular clouds.

Acknowledgements. The development of *Planck* has been supported by: ESA; CNES and CNRS/INSU-IN2P3-INP (France); ASI, CNR, and INAF (Italy); NASA and DoE (USA); STFC and UKSA (UK); CSIC, MICINN, JA, and RES (Spain); Tekes, AoF, and CSC (Finland); DLR and MPG (Germany); CSA (Canada); DTU Space (Denmark); SER/SSO (Switzerland); RCN (Norway); SFI (Ireland); FCT/MCTES (Portugal); and PRACE (EU). A description of the Planck Collaboration and a list of its members, including the technical or scientific activities in which they have been involved, can be found at `http://www.sciops.esa.int/index.php?project=planck&page=Planck_Collaboration`. The research leading to these results has received funding from the European Research Council under the European Union's Seventh Framework Programme (FP7/2007-2013) / ERC grant agreement n° 267934.

References

Alves, F. O., Franco, G. A. P., & Girart, J. M. 2008, A&A, 486, L13
André, P., Men'shchikov, A., Bontemps, S., et al. 2010, A&A, 518, L102
Arzoumanian, D., André, P., Didelon, P., et al. 2011, A&A, 529, L6
Audit, E. & Hennebelle, P. 2005, A&A, 433, 1
Basu, A. & Roy, S. 2013, MNRAS, 433, 1675
Beck, R. 2007, A&A, 470, 539
Beck, R., Fletcher, A., Shukurov, A., et al. 2005, A&A, 444, 739
Benoît, A., Ade, P., Amblard, A., et al. 2004, A&A, 424, 571
Blitz, L. & Shu, F. H. 1980, ApJ, 238, 148
Brandenburg, A. & Lazarian, A. 2013, Space Sci. Rev., 178, 163
Burkhart, B., Lazarian, A., & Gaensler, B. M. 2012, ApJ, 749, 145
Cashman, L. R. & Clemens, D. P. 2014, ApJ, 793, 126
Chandrasekhar, S. & Fermi, E. 1953, ApJ, 118, 113
Chapman, N. L., Goldsmith, P. F., Pineda, J. L., et al. 2011, ApJ, 741, 21
Chyży, K. T. 2008, A&A, 482, 755
Ciolek, G. E. & Mouschovias, T. C. 1993, ApJ, 418, 774
Clark, S. E., Peek, J. E. G., & Putman, M. E. 2014, ApJ, 789, 82
Crutcher, R. M. 2012, ARA&A, 50, 29
Crutcher, R. M., Wandelt, B., Heiles, C., Falgarone, E., & Troland, T. H. 2010, ApJ, 725, 466
Dame, T. M., Hartmann, D., & Thaddeus, P. 2001, ApJ, 547, 792
Falceta-Gonçalves, D., Lazarian, A., & Kowal, G. 2008, ApJ, 679, 537
Fiege, J. D. & Pudritz, R. E. 2000, ApJ, 544, 830
Fletcher, A., Beck, R., Shukurov, A., Berkhuijsen, E. M., & Horellou, C. 2011, MNRAS, 412, 2396
Gong, H. & Ostriker, E. C. 2011, ApJ, 729, 120
Goodman, A. A., Bastien, P., Menard, F., & Myers, P. C. 1990, ApJ, 359, 363
Goodman, A. A., Jones, T. J., Lada, E. A., & Myers, P. C. 1995, ApJ, 448, 748
Górski, K. M., Hivon, E., Banday, A. J., et al. 2005, ApJ, 622, 759
Hartmann, L., Ballesteros-Paredes, J., & Bergin, E. A. 2001, ApJ, 562, 852
Haverkorn, M. 2015, in Astrophysics and Space Science Library, Vol. 407, Astrophysics and Space Science Library, ed. A. Lazarian, E. M. de Gouveia Dal Pino, & C. Melioli, 483
Haverkorn, M., Katgert, P., & de Bruyn, A. G. 2004, A&A, 427, 169
Heiles, C. & Troland, T. H. 2005, ApJ, 624, 773
Heitsch, F., Burkert, A., Hartmann, L. W., Slyz, A. D., & Devriendt, J. E. G. 2005, ApJ, 633, L113
Heitsch, F., Stone, J. M., & Hartmann, L. W. 2009, ApJ, 695, 248
Hennebelle, P. 2013, A&A, 556, A153
Hennebelle, P., Banerjee, R., Vázquez-Semadeni, E., Klessen, R. S., & Audit, E. 2008, A&A, 486, L43
Hennebelle, P. & Falgarone, E. 2012, A&A Rev., 20, 55
Hennebelle, P. & Pérault, M. 2000, A&A, 359, 1124
Heyer, M. H. & Brunt, C. M. 2012, MNRAS, 420, 1562
Hildebrand, R. H. 1988, QJRAS, 29, 327
Hildebrand, R. H., Kirby, L., Dotson, J. L., Houde, M., & Vaillancourt, J. E. 2009, ApJ, 696, 567
Houde, M., Dowell, C. D., Hildebrand, R. H., et al. 2004, ApJ, 604, 717
Houde, M., Fletcher, A., Beck, R., et al. 2013, ApJ, 766, 49
Iacobelli, M., Burkhart, B., Haverkorn, M., et al. 2014, A&A, 566, A5
Inoue, T. & Inutsuka, S.-i. 2009, ApJ, 704, 161
Jokipii, J. R. & Parker, E. N. 1969, ApJ, 155, 777
Jones, D. O., West, A. A., & Foster, J. B. 2011, AJ, 142, 44
Jones, T. J. 1989, ApJ, 346, 728
Jones, T. J., Bagley, M., Krejny, M., Andersson, B.-G., & Bastien, P. 2015, AJ, 149, 31
Jones, T. J., Klebe, D., & Dickey, J. M. 1992, ApJ, 389, 602
Kalberla, P. M. W., Dedes, L., Kerp, J., & Haud, U. 2007, A&A, 469, 511
Kalberla, P. M. W., McClure-Griffiths, N. M., Pisano, D. J., et al. 2010, A&A, 521, A17
Koch, P. M., Tang, Y.-W., & Ho, P. T. P. 2010, ApJ, 721, 815
Lamarre, J.-M., Puget, J.-L., Ade, P. A. R., et al. 2010, A&A, 520, A9
Lazarian, A. & Vishniac, E. T. 1999, ApJ, 517, 700
Lee, H. M. & Draine, B. T. 1985, ApJ, 290, 211
Li, H., Griffin, G. S., Krejny, M., et al. 2006, ApJ, 648, 340
Li, H.-b., Fang, M., Henning, T., & Kainulainen, J. 2013, MNRAS, 436, 3707
Lin, C. C., Mestel, L., & Shu, F. H. 1965, ApJ, 142, 1431
Matthews, B. C., McPhee, C. A., Fissel, L. M., & Curran, R. L. 2009, ApJS, 182, 143
Matthews, T. G., Ade, P. A. R., Angilè, F. E., et al. 2014, ApJ, 784, 116
McClure-Griffiths, N. M., Dickey, J. M., Gaensler, B. M., Green, A. J., & Haverkorn, M. 2006, ApJ, 652, 1339
Miville-Deschênes, M.-A., Lagache, G., Boulanger, F., & Puget, J.-L. 2007, A&A, 469, 595
Mörtsell, E. 2013, A&A, 550, A80
Mouschovias, T. C. & Spitzer, Jr., L. 1976, ApJ, 210, 326
Myers, P. C. & Goodman, A. A. 1991, ApJ, 373, 509
Myers, P. C., Goodman, A. A., Gusten, R., & Heiles, C. 1995, ApJ, 442, 177
Nagai, T., Inutsuka, S.-I., & Miyama, S. M. 1998, ApJ, 506, 306
Nakamura, F. & Li, Z.-Y. 2008, ApJ, 687, 354
Ostriker, E. C., Stone, J. M., & Gammie, C. F. 2001, ApJ, 546, 980
Palmeirim, P., André, P., Kirk, J., et al. 2013, A&A, 550, A38
Patrikeev, I., Fletcher, A., Stepanov, R., et al. 2006, A&A, 458, 441
Pereyra, A. & Magalhães, A. M. 2004, ApJ, 603, 584
Planck Collaboration, Ade, P. A. R., Aghanim, N., et al. 2014, ArXiv e-prints
Planck Collaboration XIX. 2011, A&A, 536, A19
Planck Collaboration XXIV. 2011, A&A, 536, A24
Planck Collaboration I. 2014, A&A, 571, A1
Planck Collaboration II. 2014, A&A, 571, A2
Planck Collaboration V. 2014, A&A, 571, A5
Planck Collaboration VI. 2014, A&A, 571, A6
Planck Collaboration VIII. 2014, A&A, 571, A8
Planck Collaboration XI. 2014, A&A, 571, A11
Planck Collaboration XIII. 2014, A&A, 571, A13
Planck Collaboration Int. XVII. 2014, A&A, 566, A55
Planck Collaboration Int. XIX. 2014, A&A, submitted
Planck Collaboration Int. XX. 2014, A&A, submitted
Pogosyan, D., Pichon, C., Gay, C., et al. 2009, MNRAS, 396, 635
Poidevin, F., Ade, P. A. R., Angile, F. E., et al. 2014, ApJ, 791, 43
Polychroni, D., Schisano, E., Elia, D., et al. 2013, ApJ, 777, L33
Saury, E., Miville-Deschênes, M.-A., Hennebelle, P., Audit, E., & Schmidt, W. 2014, A&A, 567, A16
Schlafly, E. F. & Finkbeiner, D. P. 2011, ApJ, 737, 103
Schnitzeler, D. H. F. M., Katgert, P., & de Bruyn, A. G. 2007, A&A, 471, L21
Sofue, Y. & Reich, W. 1979, A&AS, 38, 251
Soler, J. D., Hennebelle, P., Martin, P. G., et al. 2013, ApJ, 774, 128
Tang, Y.-W., Ho, P. T. P., Koch, P. M., et al. 2009, ApJ, 700, 251
Tassis, K., Dowell, C. D., Hildebrand, R. H., Kirby, L., & Vaillancourt, J. E. 2009, MNRAS, 399, 1681
Ward-Thompson, D., Sen, A. K., Kirk, J. M., & Nutter, D. 2009, MNRAS, 398, 394
Whittet, D. C. B., Hough, J. H., Lazarian, A., & Hoang, T. 2008, ApJ, 674, 304
Wolfire, M. G., Hollenbach, D., & McKee, C. F. 2010, ApJ, 716, 1191
Zweibel, E. G. 2002, ApJ, 567, 962

Appendix A: Hessian analysis of the sky

In this appendix, we detail the implementation of the Hessian analysis on the *Planck* map of specific dust intensity at 353 GHz D_{353}. We explain how we compute the derivatives of the sky brightness in Sect. A.1. The analysis is applied to a toy model of the dust emission to quantify the impact of the data noise and to

define the threshold on the curvature we use to identify and select ridges (Sect. A.2). In Sect. A.3, we compare the orientations derived from the Hessian analysis with those obtained from an alternative method, the inertia matrix used by Hennebelle (2013) for MHD simulations.

A.1. Implementation of the Hessian analysis

A general description of the Hessian analysis is presented in Sect. 4. Here, we detail how we compute the Hessian matrix for the dust map D_{353} on its `HEALPix` grid. We compute the first derivatives of the D_{353} map by performing a bilinear interpolation. We locally fit the dust emission with a linear combination of $x = b$ and $y = l\cos(b)$ plus a constant, where l and b are the Galactic longitude and latitude. In order to well sample the computation of the derivatives, bilinear interpolation is performed on a region within a disc of 10′ radius about each pixel of the `HEALPix` map. We select roughly 30 pixels at $N_{\rm side} = 1024$, around each pixel at $N_{\rm side} = 512$. The fit, performed with no weights, is equivalent to a first-order Taylor expansion of D_{353}. We repeat this procedure on the maps of the first derivatives to obtain maps of the four elements of the Hessian matrix in Eq. (7). The orientation angle θ of the brightness structures is computed using Eq. (9).

The bilinear interpolation provides error maps for the four coefficients of the matrix, computed under the assumption that the linear model is exact, i.e. assuming that the χ^2 of the fit per degree of freedom is 1. The errors on the elements of the Hessian matrix are propagated to θ. Since Eq. (9) is non-linear, we compute the error map on θ from Gaussian realizations of the errors on the coefficients of the matrix. The uncertainty in θ, computed within bins of values of the D_{353} map, is 12.6°, independent of the intensity at 353 GHz (Fig. A.1).

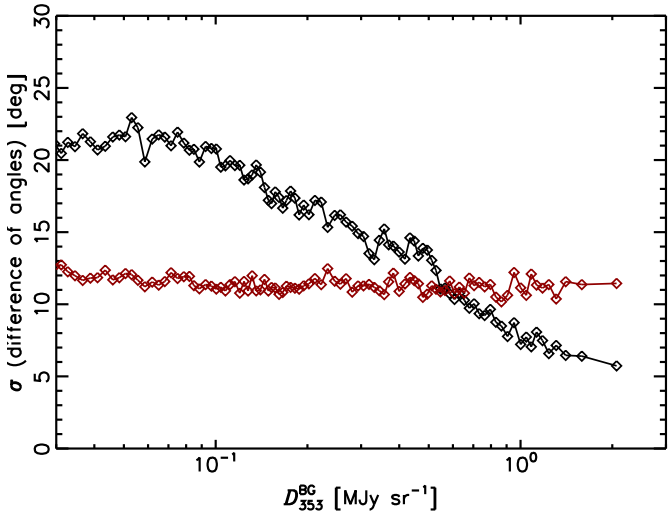

Fig. A.1. Two independent estimates of the uncertainties in the determination of angles from the Hessian analysis, computed within bins of values of the $D_{353}^{\rm BG}$ map. The red squares represent the noise obtained by propagation of the errors on the coefficients of the Hessian matrix. The noise computed with the toy model (Sect. A.2) is plotted with black squares.

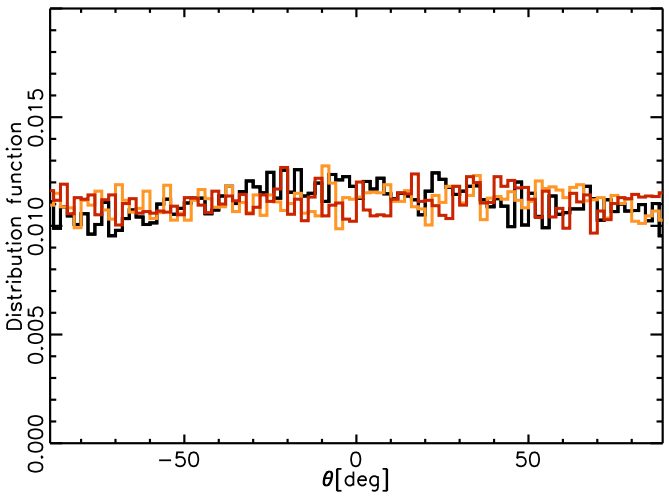

Fig. A.2. Distribution functions of orientation angles for the selected ridges derived from the Hessian analysis on T_{353}. They are computed within three bins of Galactic latitudes with equal numbers of data points. The mean absolute latitudes are 7°, 17°, and 33° for the DFs plotted in black, orange and red, respectively. The image shows that the method does not introduce any bias as a function of Galactic latitude in estimating θ.

A.2. Test on a toy model of the sky

We have tested the Hessian algorithm on a toy model of the full sky T_{353} built from a realization of a Gaussian map, $G_{\rm map}$, with an angular power spectrum, equal to a power law of index −2.8, computed with the procedure `SYNFAST` of `HEALPix` . The spectral index used is within the range of values found for power spectra of dust maps (Miville-Deschênes et al. 2007). The mean value of $G_{\rm map}$ is 0. We form,

$$T_{353} = A\,(G_{\rm map} + D)/(\sin|b| + B\,|l|) + C, \qquad \text{(A.1)}$$

where A, B, C, and D are four factors chosen to fit the latitude profile, and the longitude profile at Galactic latitude $b = 0°$, measured on the D_{353} map. The values of these factors, including their sign, depend on the realization of $G_{\rm map}$. The toy model matches the large-scale structure of the Galactic dust emission, but it does not have its filamentary structure because it is computed from an isotropic Gaussian map. It assumes that the amplitude of the brightness fluctuations at a given scale is proportional to the brightness. This is in agreement with what has been reported for the emission at 100 μm of the diffuse ISM (Miville-Deschênes et al. 2007). We use the toy model to quantify the impact of the structure of the diffuse Galactic emission and data noise on the Hessian analysis.

We run the Hessian analysis on the T_{353} map with and without data noise computed as a Gaussian realization of the noise map on D_{353}. The DFs of orientation angles, computed for the model with added noise, are flat at all Galactic latitudes, as shown in Fig. A.2. We find no bias on the angle introduced by the large-scale gradient of the emission with Galactic latitude. We use the difference between the two angle maps computed on the T_{353} map, with and without noise, to estimate the contribution of the data noise to the uncertainty in the Hessian angle (black dots in Fig. A.1). This uncertainty decreases for increasing values of T_{353} (i.e. increasing signal-to-noise ratio). The fact that it is higher than the uncertainty estimated from the errors on

the coefficients of the Hessian matrix, for most values of the sky brightness, is likely to be due to the non-Gaussian distribution of the uncertainties in θ.

The toy model is also used to determine the threshold on the curvature we adopt to select ridges in the sky. The map of negative curvature $\lambda_-(T_{353})$ computed on T_{353} shows filament-like ridges on small angular scales. We consider that the amplitude of these ridges provide an estimate of the noise on λ_- from the structure of the background emission. To quantify this noise we compute the histogram of the $\lambda_-(T_{353})$ map for 100 bins of T_{353} values, with equal numbers of data points. In Fig. A.3, we plot the 3σ of the distribution of $-\lambda_-$ versus T_{353}, and the analytical fit to these values,

$$\frac{C_{\rm T}}{\rm MJy\,sr^{-1}\,deg^{-2}} = 13\,\sqrt{0.007 + \left(\frac{T_{353}}{4\,\rm MJy\,sr^{-1}}\right)^{1.45}}. \qquad (A.2)$$

To select brightness ridges, we use $C_{\rm T}$ as a threshold on the negative curvature (see Sect. 4). The difference between the maximum and minimum eigenvalues of the Hessian matrix, λ_+ and λ_- respectively, is greater than $C_{\rm T}$ for 94 % of the selected ridges. This shows that we select elongated ridges rather than rotationally symmetric structures, for which λ_+ would be comparable with λ_-. Figure A.3 also shows the median value of $-\lambda_-$, computed on the D_{353} map within the mask defined by the contrast parameter $\zeta = 1$ in Sect. 4.2, and the power law fit

$$\frac{C_{\rm M}}{[\rm MJy\,sr^{-1}\,deg^{-2}]} = (D_{353}^{\rm BG}/[0.07\,\rm MJy\,sr^{-1}])^{0.9}. \qquad (A.3)$$

The comparison of $C_{\rm T}$ and $C_{\rm M}$ shows that our selection of ridges relies mainly on the brightness contrast. The threshold $C_{\rm T}$ on the curvature introduces a significant selection of sky pixels only for structures at high Galactic latitudes.

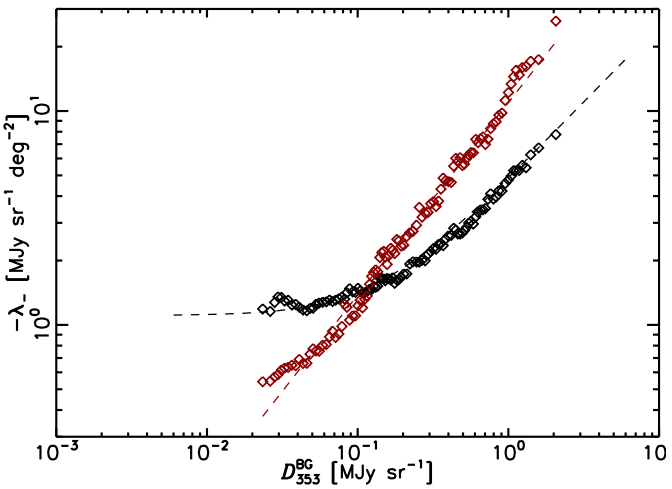

Fig. A.3. Results of a Hessian analysis of the toy model of the sky T_{353} with instrumental noise. The black (red) squares represent the 3σ level of the distribution of $-\lambda_-(T_{353})$ ($-\lambda_-(D_{353})$) within bins of $D_{353}^{\rm BG}$ computed with the mask used in our data analysis. The dashed lines represent the analytical fits in Eq. (A.2) (black dashed line) and Eq. (A.3) (red dashed line).

A.3. Comparison with an alternative method

To test the robustness of our methodology in finding the orientation θ of the ridges, we use an independent algorithm to compute the orientation of structures in the dust map. Hennebelle (2013) used the inertia matrix of the gas density to analyse structures in his MHD simulations. We adapted this method, computing the inertia matrix of the dust D_{353} map. The off-diagonal coefficients of the inertia matrix are defined as

$$I_{xy} = \sum_A \Delta x(i)\,\Delta y(i)\,K(i)\,D_{353}(i), \qquad (A.4)$$

where the sum is performed over sky pixels within an area A centred on the pixels of a `HEALPix` grid, and $\Delta x(i)$ and $\Delta y(i)$ are the offsets of the coordinates $x = b$ and $y = l\,\cos(b)$ of the pixel i with respect to the barycentre of the dust emission $x_{\rm c}$ and $y_{\rm c}$. The equations for the diagonal terms of the inertia matrix are obtained by substitution of the $\Delta x(i)\,\Delta y(i)$ product by the squares of $\Delta x(i)$ and $\Delta y(i)$ in Eq. (A.4). The coordinates of the barycentre are computed with the equations

$$x_{\rm c} = \sum_A x(i)\,K(i)\,D_{353}(i); \quad y_{\rm c} = \sum_A y(i)\,K(i)\,D_{353}(i). \qquad (A.5)$$

In Eqs. (A.4) and (A.5), $D_{353}(i)$ is the dust emission at pixel i and $K(i)$ is a kernel, which depends on the distance to the central pixel of the area A, defining the angular resolution of the computation of the inertia matrix. We use a Gaussian kernel with a full width at half maximum of 15′, which matches the angular resolution of the D_{353} map used for the computation of the Hessian matrix, and a circular area A with a diameter of 30′. A good sampling of the brightness structure within the area A is needed to compute the sum in Eq. (A.4) with the required accuracy. The orientation angle $\theta_{\rm I}$ of the brightness structures is computed using Eq. (9), where the terms of the Hessian matrix are substituted by those of the inertia matrix. When the inertia matrix is computed on a small number of pixels, the map of $\theta_{\rm I}$ shows systematic patterns associated with the `HEALPix` pixelization. To circumvent this problem, we use here for D_{353} the full resolution map of Planck Collaboration XI (2014) at 5′ resolution on a `HEALPix` grid with $N_{\rm side} = 2048$.

We computed the standard deviations of $\theta - \theta_{\rm I}$ for our selected ridges, within bins of sky brightness with equal numbers of sky pixels. We found a fixed value of about 20°, independent of the sky brightness (see the bottom panel in Fig. A.4). The probability distribution of $\theta - \theta_{\rm I}$ computed over our data selection is plotted in the top panel of Fig. A.4. It is much narrower than the distributions computed when comparing the Hessian and polarization angles in Sect. 6. Finally, we also checked that the results of our data analysis are robust against removing from the analysis the pixels in the wings of the distribution of $\theta - \theta_{\rm I}$.

Appendix B: Gaussian models

In this Appendix, we present the Gaussian models that are compared with the data in Sects. 5, 6 and 7. These models provide a framework to quantify projection effects and interpret the DFs of the angle between the magnetic field and the brightness ridges on the sky. We describe the models in Sect. B.1 and their application in Sect. B.2.

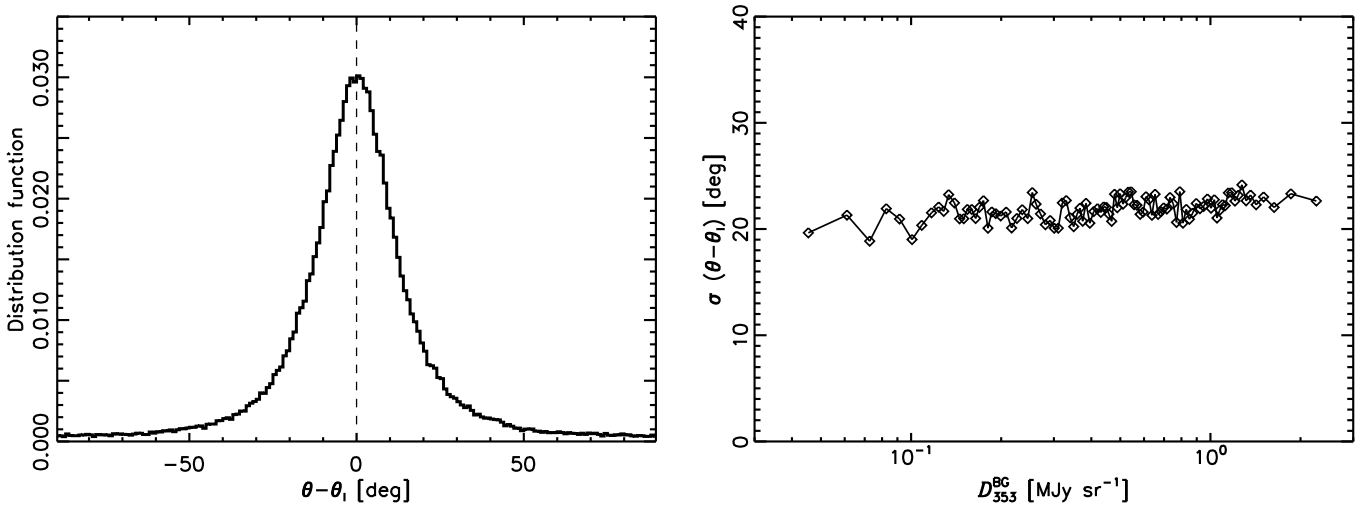

Fig. A.4. *Left*: distribution function of the difference between the angles of brightness structures in the dust emission map derived from the Hessian (θ) and inertia (θ_I) analysis. This comparison between the two independent algorithms provides the uncertainty of the Hessian angles that is smaller than the dispersion between the Hessian and polarization angles (Sect. 6). *Right*: the standard deviation of the difference between the Hessian and inertia angles ($\theta - \theta_I$) computed within bins of D_{353}^{BG}.

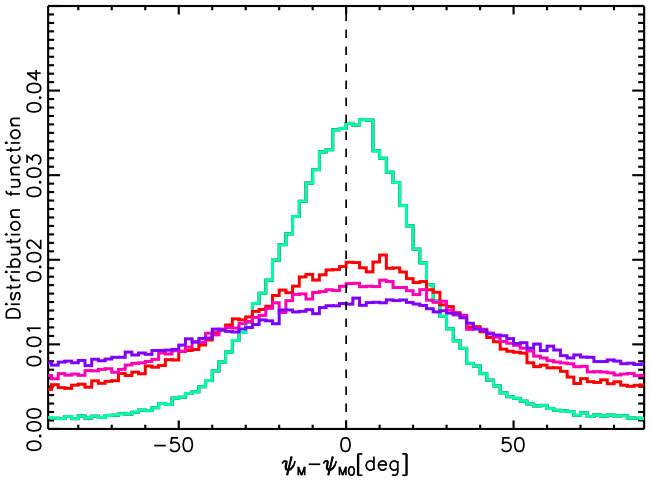

Fig. B.1. Distribution functions for the Gaussian models for four values of the dispersion of the $\boldsymbol{V}_{\rm M}$ direction about $\boldsymbol{V}_{\rm M0}$. The dispersion of angles in the models is parametrized by the value of $f_{\rm M}$ ($\sigma_{\rm M}$). It is the strongest in the purple case, $f_{\rm M} = 1.5$ ($\sigma_{\rm M} = 38°$). The other curves correspond to $f_{\rm M} = 1.2$ ($\sigma_{\rm M} = 33°$) in magenta, $f_{\rm M} = 1.0$ ($\sigma_{\rm M} = 29°$) in red, and the weakest, $f_{\rm M} = 0.5$ ($\sigma_{\rm M} = 15°$), in green. Each DF is computed over the same set of pixels used for the data analysis. The plot shows the results for the index of the power spectrum −1.5.

B.1. Description of the models

Each model is built from 3D vectors $\boldsymbol{V}_{\rm M}$ with a Gaussian distribution of orientations about a mean direction $\boldsymbol{V}_{\rm M0}$. The three components of $\boldsymbol{V}_{\rm M}$ are independent realizations of a Gaussian field on a full-sky `HEALPix` grid, at a 15′ resolution, with an angular power spectrum having a power law of index $\alpha_{\rm M}$, to which we add the components of $\boldsymbol{V}_{\rm M0}$ [5]. The mean of $\boldsymbol{V}_{\rm M}$ is $\boldsymbol{V}_{\rm M0}$. We computed several sets of models for a range of ratios $f_{\rm M}$ between the standard deviation of $|\boldsymbol{V}_{\rm M}|$ and $|\boldsymbol{V}_{\rm M0}|$, and for different values of the spectral index $\alpha_{\rm M}$. The ratio $f_{\rm M}$ determines the amplitude of the scatter of $\boldsymbol{V}_{\rm M}$ with respect to $\boldsymbol{V}_{\rm M0}$, while the spectral index $\alpha_{\rm M}$ controls the correlation across the sky of the direction of $\boldsymbol{V}_{\rm M}$. The distribution function of angles between $\boldsymbol{V}_{\rm M}$ and $\boldsymbol{V}_{\rm M0}$ per unit solid angle is close to Gaussian with a standard deviation, $\sigma_{\rm M}$, that increases from 9.°7 to 29.°5 and 38° for $f_{\rm M} = 0.3$, 1.0 and 1.5.

For each model, we compute maps of the projections of $\boldsymbol{V}_{\rm M}$ and $\boldsymbol{V}_{\rm M0}$ onto the sky with respect to the local direction of the north Galactic pole, $\psi_{\rm M}$ and $\psi_{\rm M0}$, respectively. We use the trigonometric formula in Eq. (15) to compute the difference between these angle maps with $\alpha = \psi_{\rm M}$ and $\beta = \psi_{\rm M0}$. Over the `HEALPix` grid, we sample uniformly the relative angle between the line of sight and the mean vector $\boldsymbol{V}_{\rm M0}$.

DFs of the difference of angles between the projections of $\boldsymbol{V}_{\rm M}$ and $\boldsymbol{V}_{\rm M0}$ onto the plane of the sky, computed with the same mask as that used in the data analysis, are presented, for a few models, in Fig. B.1. We show models with increasing values of $f_{\rm M}$ for a spectral index $\alpha_{\rm M} = -1.5$. Our choice of this spectral index is arbitrary because it is not tuned to reproduce power spectra computed from observations. When we use a steeper power spectrum the results are similar, although less regular and slightly asymmetric about the origin. This asymmetry arises from sample variance because, for decreasing values of $\alpha_{\rm M}$, the distribution of the $\boldsymbol{V}_{\rm M}$ direction is less sampled as a result of the correlation of $\boldsymbol{V}_{\rm M}$ on the sky. In Fig. B.2 we illustrate the effect of sample variance comparing the DFs of relative orientations of the data (see Fig. 8) with those of multiple Gaussian realizations for both $\alpha_{\rm M} = -1.5$ and $\alpha_{\rm M} = -2.0$, with a fixed value of $f_{\rm M} = 0.8$. Because of sample variance, the models for the steeper power spectrum show a larger asymmetry and skewness than those for the shallower power spectrum, and than what is observed for the data. Therefore, in the analysis, we make use of

[5] These realizations are computed with the procedure `SYNFAST` of `HEALPix` at $N_{\rm side} = 512$.

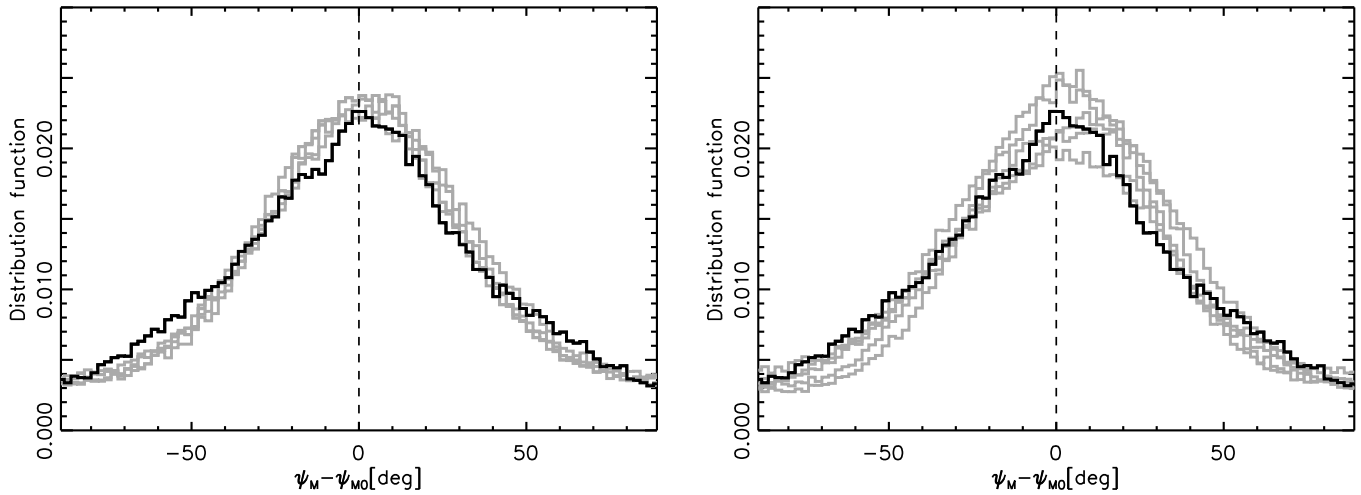

Fig. B.2. Comparison of the distribution functions of relative orientations for the data, in black (see Fig. 8), and the Gaussian models with $f_M = 0.8$, in grey, only considering the selected pixels. The two plots show five realizations of the Gaussian models with an angular power spectrum of power law index $\alpha_M = -1.5$ (*left*) and $\alpha_M = -2.0$ (*right*). Because of sample variance, the steeper power spectrum produces asymmetries and skewness in the distributions.

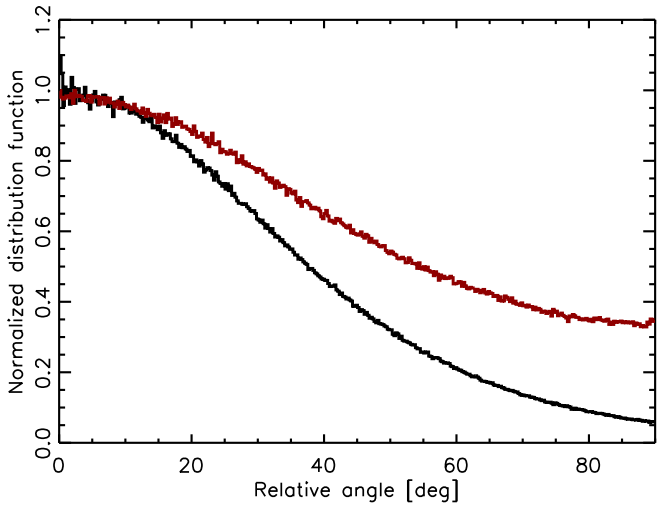

Fig. B.3. The distribution of angles between $\boldsymbol{V}_M$ and $\boldsymbol{V}_{M0}$ per unit solid angle for $f_M = 1.2$ and $\alpha_M = -1.5$, in black, is compared to the distribution of angles between the projections of the two vectors on the plane of the sky, in red. Because of projection effects the dispersion in 2D is larger than in 3D.

the Gaussian models with an angular power spectrum of power law index $\alpha_M = -1.5$. In Fig. B.3, the DF of the angle between the projections of $\boldsymbol{V}_M$ and $\boldsymbol{V}_{M0}$ is shown to be broader than that computed in 3D. The DFs in Fig. B.1 show a pedestal that extends to $-90°$ and $90°$, corresponding to positions in the sky where $\boldsymbol{V}_M$ or $\boldsymbol{V}_{M0}$ are close to the line-of-sight orientation. In this case $\boldsymbol{V}_M$ or $\boldsymbol{V}_{M0}$ are along the line of sight and the angle between the projections of the two vectors onto the plane of the sky can have any value independently of the 3D angle. The impact of projection on the DF of polarization angles has also been quantified with numerical simulations (Falceta-Gonçalves et al. 2008).

B.2. Use of the models

The Gaussian models are used in different contexts, where the vectors $\boldsymbol{V}_M$ and $\boldsymbol{V}_{M0}$ have different physical interpretations. In Sect. 5, we use the Gaussian models to interpret the DF of relative orientations between the local and mean magnetic field directions. In this case, $\boldsymbol{V}_M$ is the direction of the local field and $\boldsymbol{V}_{M0}$ that of the background field assumed to be fixed over the sky. Here, f_M is the ratio between the random, referred to as turbulent, and mean components of the magnetic field. In Sect. 6, we use the Gaussian models to interpret the DF of relative orientations between the magnetic field and ridges. In this case, $\boldsymbol{V}_M$ is the orientation of the field and $\boldsymbol{V}_{M0}$ that of the ridge. Here, the parameter of the models is σ_M, which measures the degree of alignment between the field and the ridges. In both cases, the statistics over the sky provide a homogeneous sampling of the relative orientation of the line of sight and the reference (the background magnetic field or the filaments) even when we do not introduce any variation of $\boldsymbol{V}_{M0}$ on the sky.

To study the orientations of the filaments with respect to the magnetic field, we run models with three different configurations for $\boldsymbol{V}_{M0}$. In the first case, we fix the direction of $\boldsymbol{V}_{M0}$. In the second case, we use two directions of $\boldsymbol{V}_{M0}$ perpendicular to each other, as explained in Sect. 7.2. In the third case, we run a model in which we set $\boldsymbol{V}_{M0}$ to 0 to quantify the impact of the projection when the magnetic field and the matter structures orientations are uncorrelated. This third configuration allows us to test whether or not, in the highest column density regions, the correlation between the magnetic field and the distribution of interstellar matter is lost. In Fig. B.4, we present the maps of relative orientations between ψ_M and θ, in the Taurus and Chamaeleon fields shown in Fig. 17, for one realization of this model after applying the mask described in Sect. 4.2. Although these maps show black and white patterns, which resemble the data, we do not find any elongated and coherent structures such as those in Fig. 17, like the Musca filament.

[1] APC, AstroParticule et Cosmologie, Université Paris Diderot, CNRS/IN2P3, CEA/lrfu, Observatoire de Paris, Sorbonne Paris

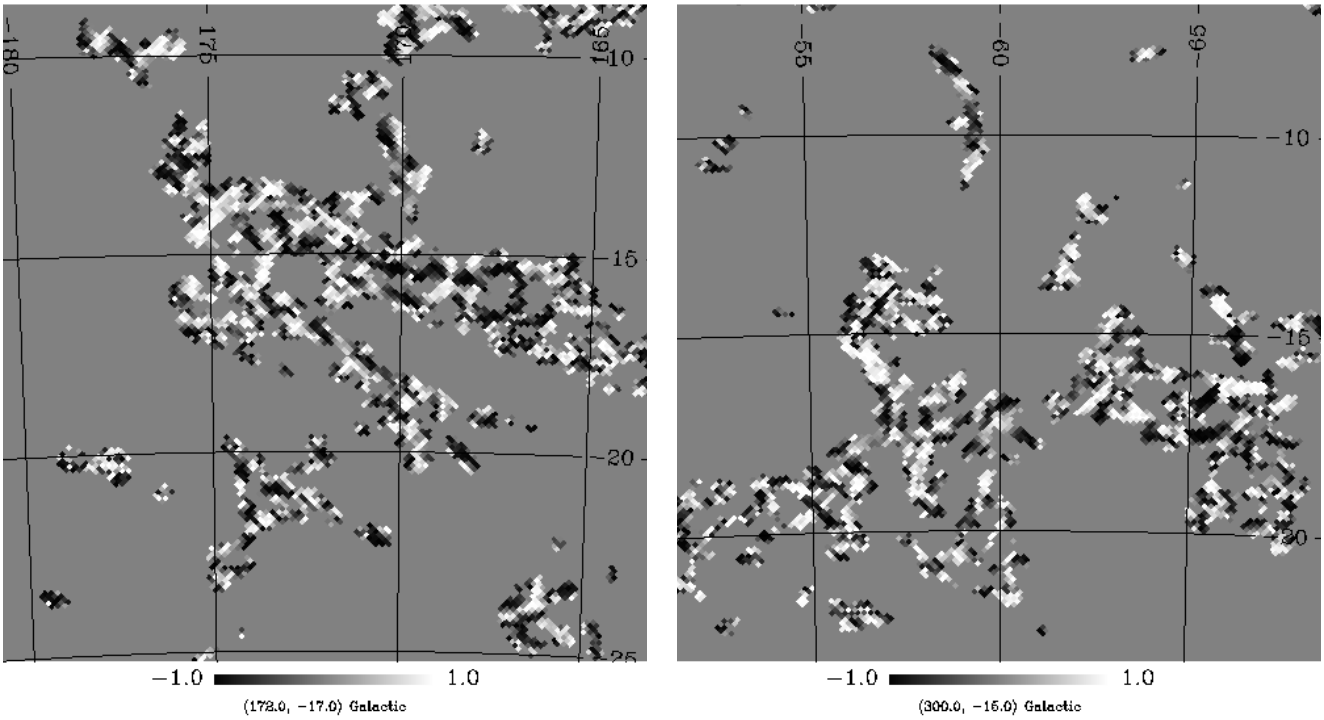

Fig. B.4. Maps of relative orientations between the orientation angle, θ, of the selected structures and the projection of $\boldsymbol{V}_{\rm M}$ onto the plane of the sky, for the Gaussian model in which $\boldsymbol{V}_{\rm M0}$ is set to 0. The mask described in Sect. 4.2 is applied. We show the two fields of view presented in Fig. 17: Taurus (*left*) and Chamaeleon (*right*) molecular complexes. The white (black) structures correspond to alignment (anti-alignment) between the projection of $\boldsymbol{V}_{\rm M}$ onto the plane of the sky and θ. This figure shows that projection effects cannot account for the elongated and coherent structures in the relative orientation maps of Fig. 17 (*right*).

Cité, 10, rue Alice Domon et Léonie Duquet, 75205 Paris Cedex 13, France
[2] African Institute for Mathematical Sciences, 6-8 Melrose Road, Muizenberg, Cape Town, South Africa
[3] Agenzia Spaziale Italiana Science Data Center, Via del Politecnico snc, 00133, Roma, Italy
[4] Agenzia Spaziale Italiana, Viale Liegi 26, Roma, Italy
[5] Aix Marseille Université, CNRS, LAM (Laboratoire d'Astrophysique de Marseille) UMR 7326, 13388, Marseille, France
[6] Astrophysics Group, Cavendish Laboratory, University of Cambridge, J J Thomson Avenue, Cambridge CB3 0HE, U.K.
[7] Astrophysics & Cosmology Research Unit, School of Mathematics, Statistics & Computer Science, University of KwaZulu-Natal, Westville Campus, Private Bag X54001, Durban 4000, South Africa
[8] Atacama Large Millimeter/submillimeter Array, ALMA Santiago Central Offices, Alonso de Cordova 3107, Vitacura, Casilla 763 0355, Santiago, Chile
[9] CITA, University of Toronto, 60 St. George St., Toronto, ON M5S 3H8, Canada
[10] CNRS, IRAP, 9 Av. colonel Roche, BP 44346, F-31028 Toulouse cedex 4, France
[11] California Institute of Technology, Pasadena, California, U.S.A.
[12] Centro de Estudios de Física del Cosmos de Aragón (CEFCA), Plaza San Juan, 1, planta 2, E-44001, Teruel, Spain
[13] Computational Cosmology Center, Lawrence Berkeley National Laboratory, Berkeley, California, U.S.A.
[14] DSM/Irfu/SPP, CEA-Saclay, F-91191 Gif-sur-Yvette Cedex, France
[15] DTU Space, National Space Institute, Technical University of Denmark, Elektrovej 327, DK-2800 Kgs. Lyngby, Denmark
[16] Département de Physique Théorique, Université de Genève, 24, Quai E. Ansermet,1211 Genève 4, Switzerland
[17] Departamento de Física, Universidad de Oviedo, Avda. Calvo Sotelo s/n, Oviedo, Spain
[18] Department of Astrophysics/IMAPP, Radboud University Nijmegen, P.O. Box 9010, 6500 GL Nijmegen, The Netherlands
[19] Department of Physics & Astronomy, University of British Columbia, 6224 Agricultural Road, Vancouver, British Columbia, Canada
[20] Department of Physics and Astronomy, Dana and David Dornsife College of Letter, Arts and Sciences, University of Southern California, Los Angeles, CA 90089, U.S.A.
[21] Department of Physics and Astronomy, University College London, London WC1E 6BT, U.K.
[22] Department of Physics, Florida State University, Keen Physics Building, 77 Chieftan Way, Tallahassee, Florida, U.S.A.
[23] Department of Physics, Gustaf Hällströmin katu 2a, University of Helsinki, Helsinki, Finland
[24] Department of Physics, Princeton University, Princeton, New Jersey, U.S.A.
[25] Department of Physics, University of California, Santa Barbara, California, U.S.A.
[26] Department of Physics, University of Illinois at Urbana-Champaign, 1110 West Green Street, Urbana, Illinois, U.S.A.
[27] Dipartimento di Fisica e Astronomia G. Galilei, Università degli Studi di Padova, via Marzolo 8, 35131 Padova, Italy
[28] Dipartimento di Fisica e Scienze della Terra, Università di Ferrara, Via Saragat 1, 44122 Ferrara, Italy

[29] Dipartimento di Fisica, Università La Sapienza, P. le A. Moro 2, Roma, Italy
[30] Dipartimento di Fisica, Università degli Studi di Milano, Via Celoria, 16, Milano, Italy
[31] Dipartimento di Fisica, Università degli Studi di Trieste, via A. Valerio 2, Trieste, Italy
[32] Dipartimento di Fisica, Università di Roma Tor Vergata, Via della Ricerca Scientifica, 1, Roma, Italy
[33] Discovery Center, Niels Bohr Institute, Blegdamsvej 17, Copenhagen, Denmark
[34] Dpto. Astrofísica, Universidad de La Laguna (ULL), E-38206 La Laguna, Tenerife, Spain
[35] European Southern Observatory, ESO Vitacura, Alonso de Cordova 3107, Vitacura, Casilla 19001, Santiago, Chile
[36] European Space Agency, ESAC, Planck Science Office, Camino bajo del Castillo, s/n, Urbanización Villafranca del Castillo, Villanueva de la Cañada, Madrid, Spain
[37] European Space Agency, ESTEC, Keplerlaan 1, 2201 AZ Noordwijk, The Netherlands
[38] Facoltà di Ingegneria, Università degli Studi e-Campus, Via Isimbardi 10, Novedrate (CO), 22060, Italy
[39] HGSFP and University of Heidelberg, Theoretical Physics Department, Philosophenweg 16, 69120, Heidelberg, Germany
[40] Helsinki Institute of Physics, Gustaf Hällströmin katu 2, University of Helsinki, Helsinki, Finland
[41] INAF - Osservatorio Astrofisico di Catania, Via S. Sofia 78, Catania, Italy
[42] INAF - Osservatorio Astronomico di Padova, Vicolo dell'Osservatorio 5, Padova, Italy
[43] INAF - Osservatorio Astronomico di Roma, via di Frascati 33, Monte Porzio Catone, Italy
[44] INAF - Osservatorio Astronomico di Trieste, Via G.B. Tiepolo 11, Trieste, Italy
[45] INAF/IASF Bologna, Via Gobetti 101, Bologna, Italy
[46] INAF/IASF Milano, Via E. Bassini 15, Milano, Italy
[47] INFN, Sezione di Bologna, Via Irnerio 46, I-40126, Bologna, Italy
[48] INFN, Sezione di Roma 1, Università di Roma Sapienza, Piazzale Aldo Moro 2, 00185, Roma, Italy
[49] INFN/National Institute for Nuclear Physics, Via Valerio 2, I-34127 Trieste, Italy
[50] IPAG: Institut de Planétologie et d'Astrophysique de Grenoble, Université Grenoble Alpes, IPAG, F-38000 Grenoble, France, CNRS, IPAG, F-38000 Grenoble, France
[51] Imperial College London, Astrophysics group, Blackett Laboratory, Prince Consort Road, London, SW7 2AZ, U.K.
[52] Infrared Processing and Analysis Center, California Institute of Technology, Pasadena, CA 91125, U.S.A.
[53] Institut Universitaire de France, 103, bd Saint-Michel, 75005, Paris, France
[54] Institut d'Astrophysique Spatiale, CNRS (UMR8617) Université Paris-Sud 11, Bâtiment 121, Orsay, France
[55] Institut d'Astrophysique de Paris, CNRS (UMR7095), 98 bis Boulevard Arago, F-75014, Paris, France
[56] Institute for Space Sciences, Bucharest-Magurale, Romania
[57] Institute of Astronomy, University of Cambridge, Madingley Road, Cambridge CB3 0HA, U.K.
[58] Institute of Theoretical Astrophysics, University of Oslo, Blindern, Oslo, Norway
[59] Instituto de Astrofísica de Canarias, C/Vía Láctea s/n, La Laguna, Tenerife, Spain
[60] Instituto de Física de Cantabria (CSIC-Universidad de Cantabria), Avda. de los Castros s/n, Santander, Spain
[61] Jet Propulsion Laboratory, California Institute of Technology, 4800 Oak Grove Drive, Pasadena, California, U.S.A.
[62] Jodrell Bank Centre for Astrophysics, Alan Turing Building, School of Physics and Astronomy, The University of Manchester, Oxford Road, Manchester, M13 9PL, U.K.
[63] Kavli Institute for Cosmology Cambridge, Madingley Road, Cambridge, CB3 0HA, U.K.
[64] LAL, Université Paris-Sud, CNRS/IN2P3, Orsay, France
[65] LERMA, CNRS, Observatoire de Paris, 61 Avenue de l'Observatoire, Paris, France
[66] Laboratoire AIM, IRFU/Service d'Astrophysique - CEA/DSM - CNRS - Université Paris Diderot, Bât. 709, CEA-Saclay, F-91191 Gif-sur-Yvette Cedex, France
[67] Laboratoire Traitement et Communication de l'Information, CNRS (UMR 5141) and Télécom ParisTech, 46 rue Barrault F-75634 Paris Cedex 13, France
[68] Laboratoire de Physique Subatomique et de Cosmologie, Université Joseph Fourier Grenoble I, CNRS/IN2P3, Institut National Polytechnique de Grenoble, 53 rue des Martyrs, 38026 Grenoble cedex, France
[69] Laboratoire de Physique Théorique, Université Paris-Sud 11 & CNRS, Bâtiment 210, 91405 Orsay, France
[70] Lawrence Berkeley National Laboratory, Berkeley, California, U.S.A.
[71] Max-Planck-Institut für Astrophysik, Karl-Schwarzschild-Str. 1, 85741 Garching, Germany
[72] Max-Planck-Institut für Radioastronomie, Auf dem Hügel 69, 53121 Bonn, Germany
[73] McGill Physics, Ernest Rutherford Physics Building, McGill University, 3600 rue University, Montréal, QC, H3A 2T8, Canada
[74] National University of Ireland, Department of Experimental Physics, Maynooth, Co. Kildare, Ireland
[75] Niels Bohr Institute, Blegdamsvej 17, Copenhagen, Denmark
[76] Observational Cosmology, Mail Stop 367-17, California Institute of Technology, Pasadena, CA, 91125, U.S.A.
[77] Optical Science Laboratory, University College London, Gower Street, London, U.K.
[78] SISSA, Astrophysics Sector, via Bonomea 265, 34136, Trieste, Italy
[79] School of Physics and Astronomy, Cardiff University, Queens Buildings, The Parade, Cardiff, CF24 3AA, U.K.
[80] Space Research Institute (IKI), Russian Academy of Sciences, Profsoyuznaya Str, 84/32, Moscow, 117997, Russia
[81] Space Sciences Laboratory, University of California, Berkeley, California, U.S.A.
[82] Special Astrophysical Observatory, Russian Academy of Sciences, Nizhnij Arkhyz, Zelenchukskiy region, Karachai-Cherkessian Republic, 369167, Russia
[83] Sub-Department of Astrophysics, University of Oxford, Keble Road, Oxford OX1 3RH, U.K.
[84] UPMC Univ Paris 06, UMR7095, 98 bis Boulevard Arago, F-75014, Paris, France
[85] Université de Toulouse, UPS-OMP, IRAP, F-31028 Toulouse cedex 4, France
[86] Universities Space Research Association, Stratospheric Observatory for Infrared Astronomy, MS 232-11, Moffett Field, CA 94035, U.S.A.
[87] University of Granada, Departamento de Física Teórica y del Cosmos, Facultad de Ciencias, Granada, Spain
[88] University of Granada, Instituto Carlos I de Física Teórica y Computacional, Granada, Spain
[89] Warsaw University Observatory, Aleje Ujazdowskie 4, 00-478 Warszawa, Poland